

Characterization and Monte Carlo evaluation of positioning uncertainty of an MAFM.

Master's thesis, 6.2.2019

Author:

JOHAN CHRISTOFFER NYSTEN

Supervisors:

VIRPI KORPELAINEN (VTT MIKES)

VESA APAJA (JYU)



UNIVERSITY OF JYVÄSKYLÄ
DEPARTMENT OF PHYSICS

© 2019 Johan Christoffer Nysten

Julkaisu on tekijänoikeussäännösten alainen. Teosta voi lukea ja tulostaa henkilökohtaista käyttöä varten. Käyttö kaupallisiin tarkoituksiin on kielletty. This publication is copyrighted. You may download, display and print it for Your own personal use. Commercial use is prohibited.

Abstract

Nysten, Johan

Characterization and Monte Carlo evaluation of positioning uncertainty of an MAFM
Master's thesis

Department of Physics, University of Jyväskylä, 2018, 64 pages.

Traceability to the SI metre is the basis for dimensional measurements in the nanometer scale. Atom Force Microscopes (AFMs) are used to measure surface features with subnanometre resolution. Metrological AFMs (MAFMs) use interferometers for positioning, making surface measurements directly traceable. The MIKES MAFM was further developed under the EMPiR initiative's 3DNano project. The device's largest uncertainty sources were characterized and modeled as part of this thesis, and used to construct a system model in Matlab. Evaluating the system model using a simple Monte Carlo method gives us the standard uncertainty components for 3D positioning. Some uncertainty sources, such as interferometer target mirror flatness, were qualitatively analyzed but not modeled. Preliminary results were generated using surface points of computer-generated 2D lattice, and 1×10^5 Monte Carlo trials. The computed uncertainties were all in the nm range. Development of the model will continue, with the goal of evaluating uncertainty for a measurand such as grating pitch or step height.

Keywords: Metrology, AFM, Monte Carlo, Measurement uncertainty

Tiivistelmä

Nysten, Johan

MAFM:n epävarmuuslähteiden karakterisointi ja simulointi Monte Carlo–menetelmällä

Pro gradu -tutkielma

Fysiikan laitos, Jyväskylän yliopisto, 2018, 64 sivua

Nanometrin skaalan pituus-mittaukset pohjautuvat jäljitettävyyteen, ja SI-järjestelmän metriin. Atomivoimamikroskooppeja (AFM) käytetään pintojen mittaukseen alle nanometrin erottelukyvyllä. Metrologiset AFM:t (MAFM:t) käyttävät interferometrejä paikan määrittämiseen, jolloin pinta-mittauksen ovat suoraan jäljitettäviä. MIKES MAFM jatkokehitettiin EMPIR-aloitteen 3DNano-projektin puitteissa. Tässä gradussa laitteen suurimmat epävarmuuden lähteet kartoitettiin ja mallinnettiin. Järjestelmää kuvaava malli kehitettiin Matlab:illa. Järjestelmän mallin avulla laskettiin, Monte Carlo–menetelmää käyttäen, 3D kordinaatiston epävarmuudet. Joitain epävarmuuden lähteitä ei mallinnettu, mutta näitä tarkasteltiin silti laadullisesti. Alustavat tulokset laskettiin ohjelmallisesti tuotetulle 2D hilarakenteelle, 1×10^5 Monte Carlo –iteraatiolla. Lasketut epävarmuudet jäivät nm-suuruusluokkaan. Järjestelmän mallin kehitys tulee jatkumaan, jolloin tavoitteeksi tulee mittasuureen epävarmuuden laskeminen, esim. hilan jaksolle tai askelkorkeudelle.

Avainsanoja: Metrologia, AFM, Monte Carlo, Mittausepävarmuus

Contents

Abstract	3
Tiivistelmä	5
1 Introduction	9
1.1 Metrology	9
1.2 Expression of uncertainty	10
1.3 Acknowledgements	10
2 Nanoscale dimensional metrology	13
2.1 Interferometric length measurement	13
2.2 The metrological atomic force microscope (MAFM)	18
2.3 MAFM surface measurements	23
3 Expression of uncertainty and Monte Carlo	25
3.1 Notation	25
3.2 Standard framework for expressing uncertainty	26
3.3 Simple Monte Carlo	28

3.4	Application of Monte Carlo to measurement uncertainty	30
4	System model and uncertainty	33
4.1	Abbe error	33
4.1.1	Rotations of the XY-stage	37
4.1.2	Rotations of the Z-stage	44
4.2	Interferometer non-orthogonality	45
4.3	Mirror flatness	47
4.4	Monte Carlo uncertainty evaluation	51
5	Discussion	57
6	Conclusions	59
	References	59

1 Introduction

This introduction serves to outline the motivation for this work, and underline some of technical background. Main focuses of the thesis are traceable nanoscale length measurement, and the construction of a numerical uncertainty model.

1.1 Metrology

Metrology is the science of measurement, both from theoretical and practical aspects. In industry, the proper functioning of machinery is reliant on precise and accurate measurements. In science, maintaining a common system of units is required for comparability and reliability of results. In both fields, decisions are made based on measurement results. Reliable measurement is thus central to avoiding all sorts of judicial and practical issues.

Results are made reliable through a property known as traceability. A measurement should, through an unbroken chain of comparisons, be comparable with a base unit. The base units are defined by the International System of units (SI), and comparisons are overseen by a hierarchy of metrological institutes and laboratories. It is by traceability that measurement results can be compared, reproduced, and used to derive other results.

A Metrological Atomic Force Microscope (MIKES MAFM) was built at MIKES, for the purpose of traceable nanoscale dimensional measurements. Given such capabilities, VTT MIKES can provide calibration of AFMs (and other devices) used in industry and research. This is realized in practice through the development of both the device and measurement techniques. Traceability of the instrument comes through interferometers, which provide the measurement coordinates.

1.2 Expression of uncertainty

The Guide to expression of Uncertainty in Measurement (GUM)[1] is a commonly used standard in metrology. It contains guidelines on how to estimate uncertainty using various types of parameters, given some knowledge about their distribution. It defines standard uncertainty, a concept that is familiar to most science students. The standard method of expressing uncertainty uses the Taylor expansion of a mathematical model function. Some models are non-linear, and may contain hundreds of parameters, in which case the analytical expressions become difficult to work with.

Monte Carlo methods are proven tools for statistical analysis of otherwise impermeable or cumbersome physical phenomena. For metrology, Monte Carlo provides a way to obtain measurement uncertainty without resorting to difficult analytical expressions. Even the notion of having a model in form of an equation can be relaxed, as Monte Carlo works just as well when the model lacks a closed form, but is still deterministic[2]. In fact, standard procedures for expression of uncertainty using Monte Carlo are already outlined in the GUM supplement 1[3].

1.3 Acknowledgements

The thesis, the practical work, and analysis were done at VTT MIKES, the national metrology institute in Espoo Finland. I would like to thank my primary advisor, Virpi Korpelainen from VTT MIKES, whose expertise and motivation were instrumental to the completion of this work. I also thank my advisor at University of Jyväskylä, Vesa Apaja, with whom I discussed the implementation of Monte Carlo. I would also like to thank (in no specific order) Björn Hemming, Ville Heikkinen, Jeremias Seppä, Asko Rantanen and Ville Byman for advice, practical help, and exchange of ideas. A big thank you goes also to team leader Antti Lassila.

Funding was provided by the 3DNano project[4], whose goal is the development of techniques and instruments for traceable 3D nanoscale measurements. This project has received funding from the EMPIR programme co-financed by the Participating States and from the European Union's Horizon 2020 research and innovation

programme.

2 Nanoscale dimensional metrology

This section presents dimensional metrology - length metrology - and its application for nanoscale length measurements. Traceability of nanoscale measurements is explained, in a brief overview of interferometry. Finally, the operating principle of the MIKES MAFM is shown.

2.1 Interferometric length measurement

Metrological traceability[5] is the “property of a measurement result whereby the result can be related to a reference through a documented unbroken chain of calibrations, each contributing to the measurement uncertainty”. This means that traceable measurements’ results can, by proxy, be expressed in terms of a base unit, with compounding uncertainty. The base units are defined in the International System of Units (SI), which serves as a common base for comparability, reliability and repeatability of measurements. National metrology institutes (NMIs), such as VTT MIKES, are responsible for maintaining the corresponding national standards and possibly their realization. NMIs also provide calibration services, whereby measurement devices can, through the national standards, be made fully traceable.

Traceability in length measurements starts with the SI definition of the metre. The definition goes back to the late 1800’s, when the International Metre Commission was established. To facilitate trade and comparison of measurements, an international metre standard was to be constructed. The original standard was realized as a platinum bar, which was used as a reference. Later, the invention of interferometry would help replace this standard. A first measurement of the standard metre in terms of light wavelength was made in 1892-93. By the 1960’s, the metre had been redefined in terms of vacuum wavelength of radiation from a specific transition

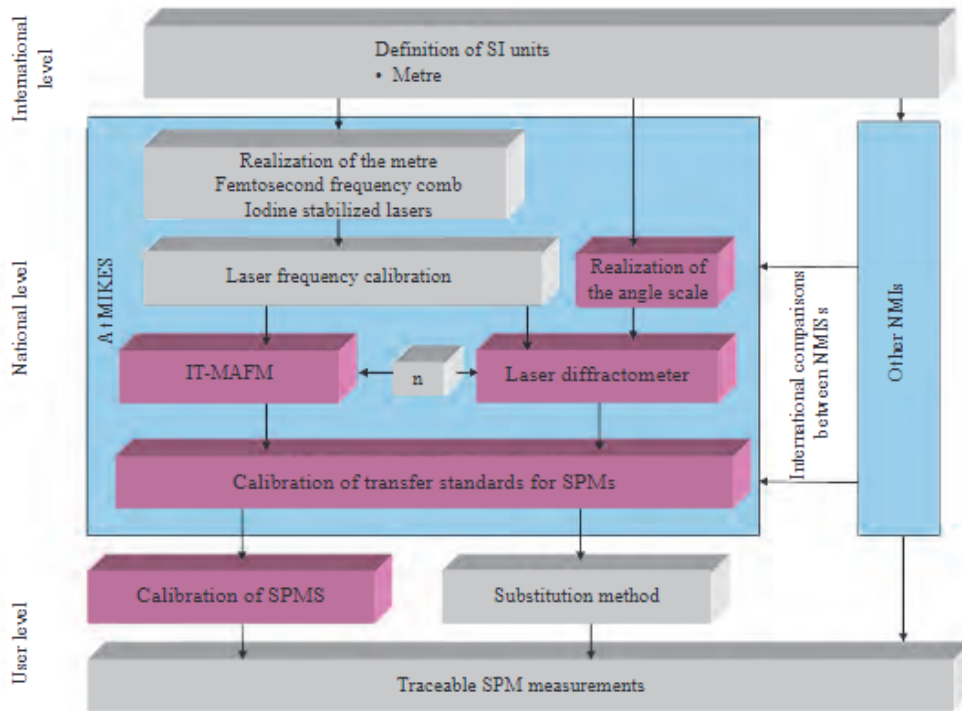


Figure 1. Traceability chain for AFM/SPM length measurements . The device is calibrated using a transfer standard, which in turn is calibrated by an NMI such as VTT MIKES [8].

in Krypton-86. The current metre definition, establish in 1983, uses the defined constant speed of light in vacuum :

Definition 2.1 *Metre is the length of the path travelled by light in vacuum during a time interval of $1/299792458$ of a second.*

A practical realization of the SI metre has existed since 1983. The metre can be realized by comparison against a standard frequency, taken from a list of recommended radiations (see e.g.[6]). At VTT MIKES, an optical frequency comb[7] is first referenced to an atomic clock of a standard frequency (hyperfine transition of Caesium-133). A stabilized laser source, characterized using the comb, is then used to calibrate an interferometer laser source. This forms the traceability chain for interferometric length measurements (fig. 1).

Traceability in length measurements is commonly realized by interferometry. The

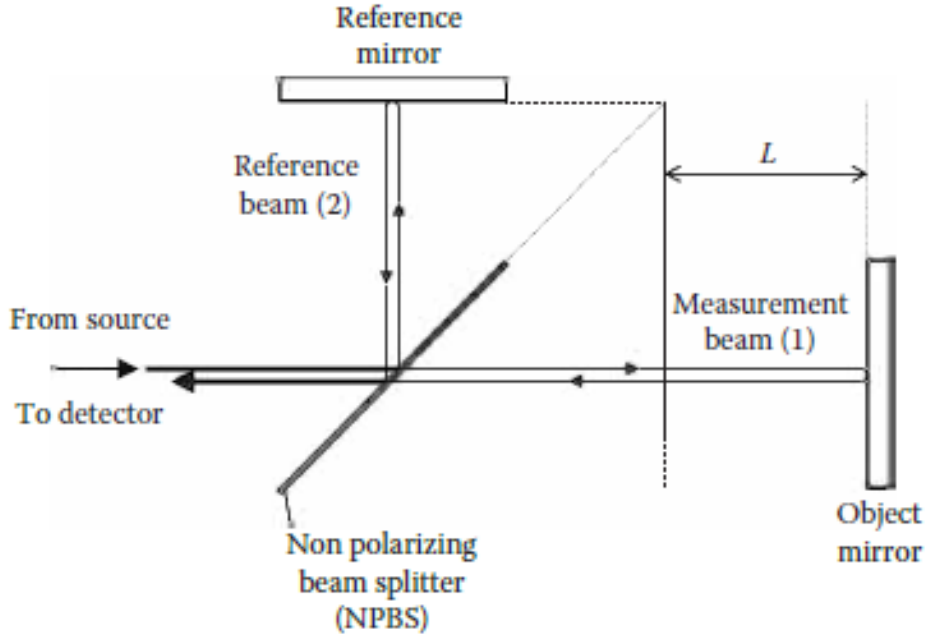


Figure 2. Simple Michelson-type interferometer[9].

Michelson interferometer, shown in fig. 2, is a simple device for measuring the displacement of a movable plane mirror. A laser beam is directed at a non-polarizing beam splitter (NPBS), a partially reflecting, partially transmitting optical component. The beam thus splits, and travels along each arm to a plane mirror. Beams from the reference arm (with a static mirror) and the measurement arm (with a mobile mirror) then pass the NPBS a second time. Interference of the re-combined beams is seen at the detector, from which the relative phase can be inferred. In a plane-wave approximation, the intensity of light at detector is[9]:

$$I = |E_{1,0}|^2 + |E_{2,0}|^2 + |E_{1,0}||E_{2,0}| \underbrace{\cos\left(4\pi\frac{L}{\lambda}\right)}_{\phi(L,\lambda)}, \quad (1)$$

where $L = (z_2 - z_1)/2$ is the difference in distance to the mirrors, and z_i the optical path of beam i .

Eq. 1 shows that due to interference, detected intensity has a period of $\lambda/2$ with respect to displacement. The transition between an intensity maxima and minima is commonly termed ‘fringe’. During a continuous movement of the measurement mirror in fig. 2, counting the number of fringes passed gives an estimate of displacement.

However, to obtain a resolution better than $\lambda/2$, fringe interpolation, i.e. phase data, is needed. In nanoscale measurements, where typically $\lambda \approx 633$ nm, this leads to a small periodic nonlinearity in measurement. One method of correcting the nonlinearity is to compare interferometer readout with a reference sensor, e.g. a capacitive sensor[10].

When used in regular laboratory conditions, interferometers are susceptible to environmental variations. Refractive index of air depends on temperature, pressure, which affects the laser wavelength:

$$\lambda = \frac{\lambda_0}{n(T, p, \dots)} \quad (2)$$

Variations are partly compensated for by placing the measurement and reference arms in fig. 2 close together and in the same direction. By monitoring environmental variables along beam path, the variation in n can be calculated[11]. However, Dead Path error occurs if the null point (point of zero measured displacement) is set at non-zero displacement. Then, part of the beam path will be rendered ‘invisible’ to refractive index corrections - in fig. 2, this amounts to fixing measurement zero at displacement L .

A variation on the interferometer is presented in fig. 3. The laser source is heterodyne: two linearly polarized and mutually orthogonal beams, with slightly different frequencies, are emitted. A polarizing beam splitter (PBS) separates the polarizations, and sends them off to the reference / measurement arm. A quarter-wave plate (QWP), rotated by 45° around the beam axis, converts between linear and circular polarization. Returning to the PBS, the beam’s polarization has been rotated by 90° . Then, the beam is reflected by the corner cube reflector (CCR), and passed again to the plane mirror before reaching detector.

The above interferometer configuration, termed ‘double-pass heterodyne differential’, can also be adapted for single-passing. By simply removing the CCR and QWPs, each beam travels only once to the respective mirror.

Summarizing, traceable length measurement is realized by interferometry, through determination of wavelength and refractive index of air. Interferometer laser is

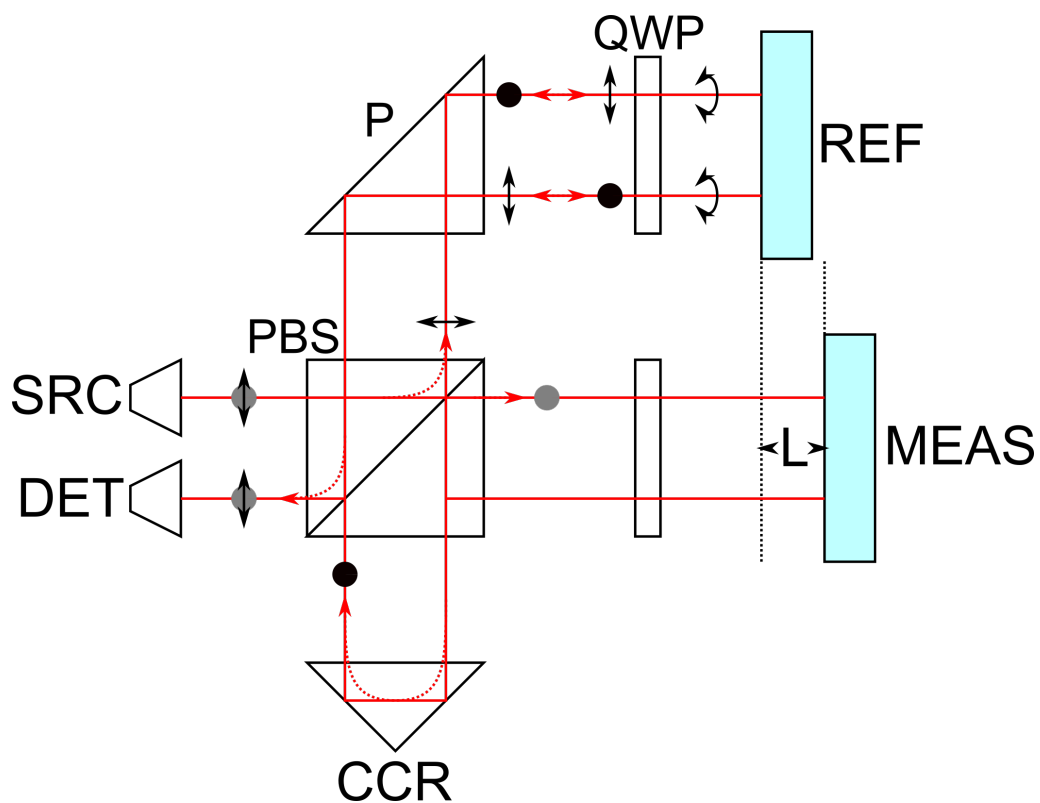


Figure 3. Heterodyne double-pass differential interferometer. SRC = source, PBS = polarizing beam splitter, CCR = corner cube reflector, P = prism, QWP = quarter-wave plate, REF = reference mirror, MEAS = measurement mirror, L = displacement. Reference beam is marked in red, and its direction with dashed line and arrow. Polarization of beam is indicated by black/grey markings: circular arc for circular polarization, disc / top-down arrow for linear.

calibrated against an iodine-stabilized laser, whose frequency is determined by optical frequency comb and an atomic clock (which realizes the SI second).

2.2 The metrological atomic force microscope (MAFM)

Atomic Force Microscopes (AFMs) are high resolution imaging devices equipped with a physical probe. The original design by Gerd Binnig[12] combined the principles of the Scanning Tunneling Microscope (STM) and the stylus profilometer. STM probes use tunneling current for imaging, and their use is thus restricted by sample material. In his design, Binnig used an STM to determine deflection of a probe that touches sample surface. Surface height is imaged by having the probe follow the surface profile, and measuring vertical deflection. Height is sampled at fixed positions, and the forming a raster image - height values on a (nominally) regular grid.

The AFM probe contains a sensitive cantilever, to which a sharp tip is mounted. As the probe is brought close to a sample, surface forces acting on the tip cause the cantilever to deflect. Deflection is measured, and in typical operation used as feedback for vertical positioning. Probe can be kept at fixed distance from surface using this feedback. Thus, the probe will maintain constant distance from a surface, and the probe's position can be monitored to obtain a surface image.

The Akiyama-probe[13] is an example of a modern probe, used in non-contact AFMs (explained in fig. 5). Tip and cantilever are attached to a quartz tuning fork, and forced to oscillate (see fig. 4). Tip-surface interaction couples into the oscillation, changing the response to driving signal. The response is measured - not deflection - making the probe 'self-sensing'.

Interaction with sample occurs through surface forces, and is thus affected by both tip design and surface characteristics[14]. True to its name, the AFM measures force, which is reflected in the generated image. Fig. 6 shows qualitatively the surface profile as measured by an AFM probe, using different models for surface force. Nominally, surface height is determined by Van der Waals force (fig. 5).

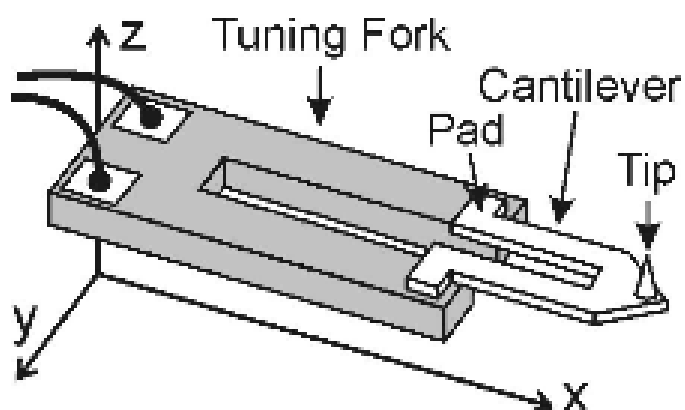


Figure 4. The Akiyama-probe, which consists of a quartz tuning fork and attached cantilever-tip-assembly. Tip-surface interaction is measured as the response to the fork's driving frequency.

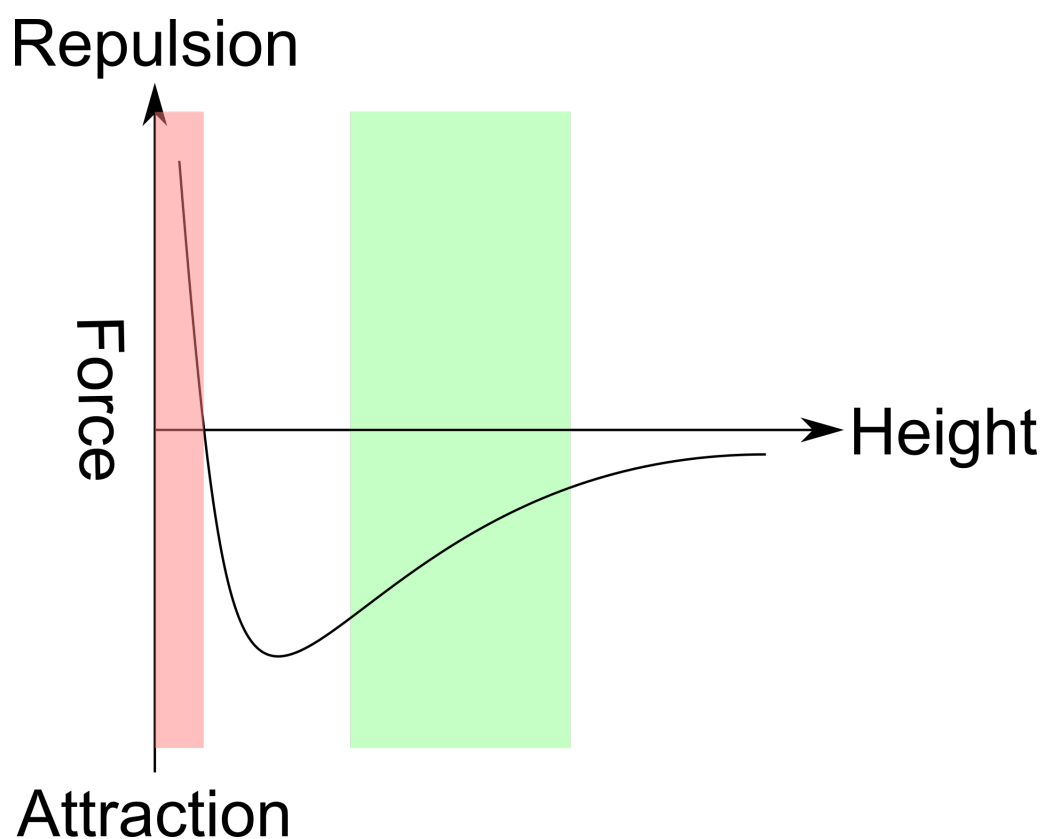


Figure 5. Van der Waals force, plotted vs. surface distance. Also shown are operational modes of AFM: contact-mode in the repulsive regime (red), non-contact mode in attractive (green).

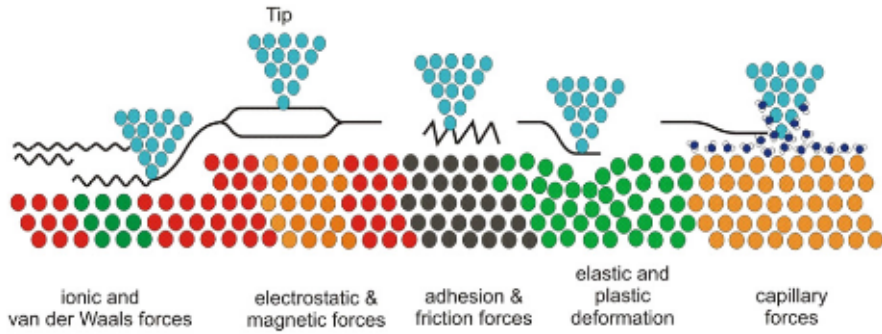


Figure 6. Some interaction forces between an AFM tip and sample surface[14].

Metrological AFMs (MAFMs) feature interferometric positioning. MAFM measurements are thus directly traceable to the SI metre, and can be used for calibrating transfer standards[8]. The transfer standard, when used to calibrate an AFM, provides the necessary traceability in measurement.

The MAFM built at VTT MIKES (the MIKES MAFM) uses two piezoelectric flexure stages to provide effective 3D motion of the probe (fig. 7). Motion of sample (in XY-plane) is supplied by a single piezoelectric flexure stage, while the probe is moved vertically (in Z) by a separate stage. Motion of the sample follows a typical raster scan path: linear traces along a single axis, incrementally offset along the other axis. Vertical position of probe follows the surface, and is read at fixed locations. The full surface image is assembled from individual profiles, or traces. Use of other scan patterns has also been investigated for high-speed AFMs, e.g. spiral paths[15].

The MIKES MAFM's scales are realized using interferometers (the red arrows marked 'ref' and 'meas' in fig. 3 connect to fig. 7). Displacement in the XY-plane is measured by two differential heterodyne double-pass interferometers, while Z-displacement is measured by two single-pass interferometers. Motion stages use displacement as feedback for positioning. XY-position is updated until the difference between target and interferometric displacement becomes sufficiently small. Z-motion uses feedback to maintain constant probe-surface separation, and surface height can thus be taken as Z-displacement.

The configuration of fig. 7 is designed to minimize errors from e.g. thermally induced changes in the frame. Fig. 8 shows the metrology loop for X-displacement

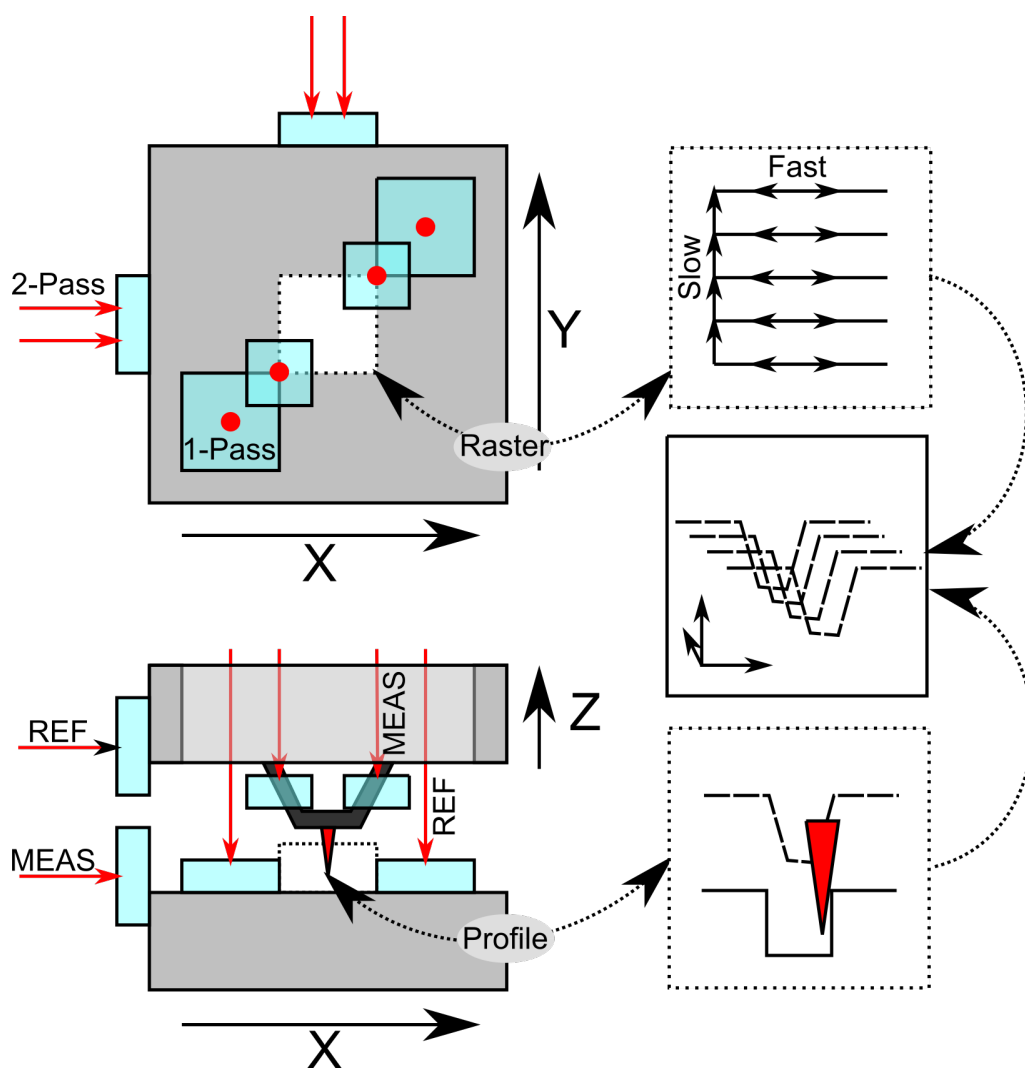


Figure 7. Positioning system of the MIKES MAFM, and principle of imaging. Sample is moved in the XY-plane, while tip moves along Z as it traces the surface. Individual linear profiles are combined to generate a surface image.

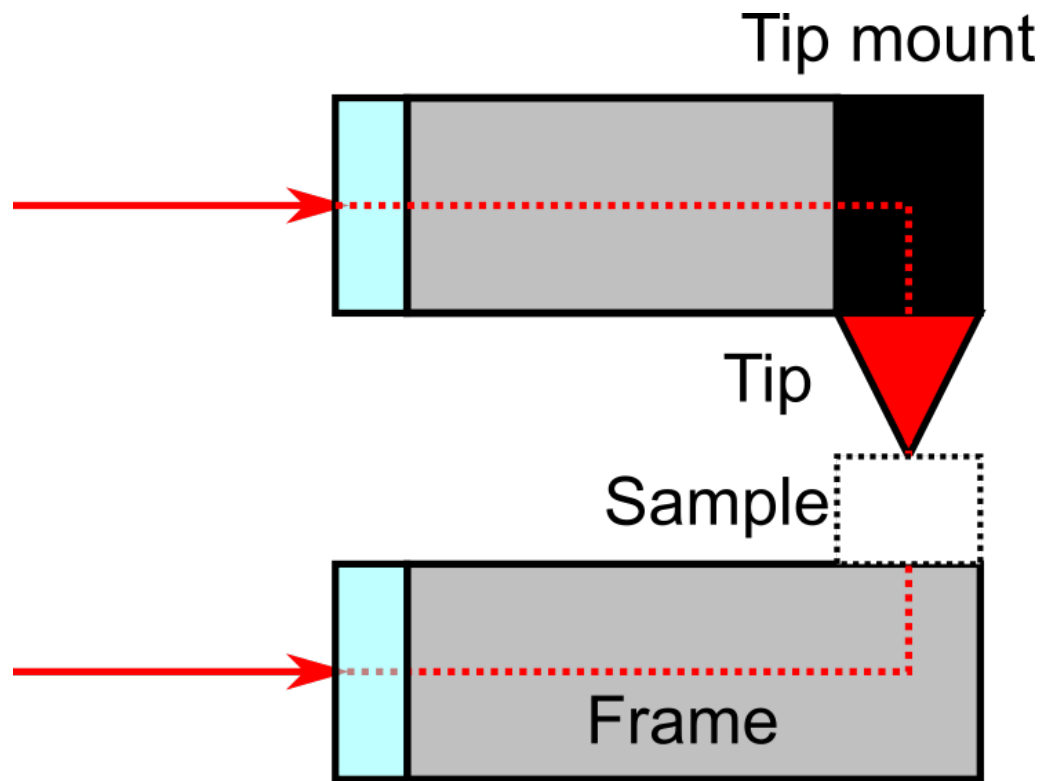


Figure 8. Metrology loop(s) for X-displacement of the MIKES MAFM (dotted red line). Interferometers ‘see’ only the displacement of plane mirrors (cyan), and are essentially blind to changes along the loop.

measurement, i.e. the fictitious line connecting sample to X-interferometer. Changes along the loop, e.g. thermal contraction/expansion or mechanical vibration, cannot be distinguished from measurement. The solution is to keep the loop as small as possible[16]. An improvement over the previously used MAFM [17], is that the Z-axis metrology loop has been shortened.

Summarizing, MAFMs are imaging microscopes with directly traceable, interferometric, length scales.

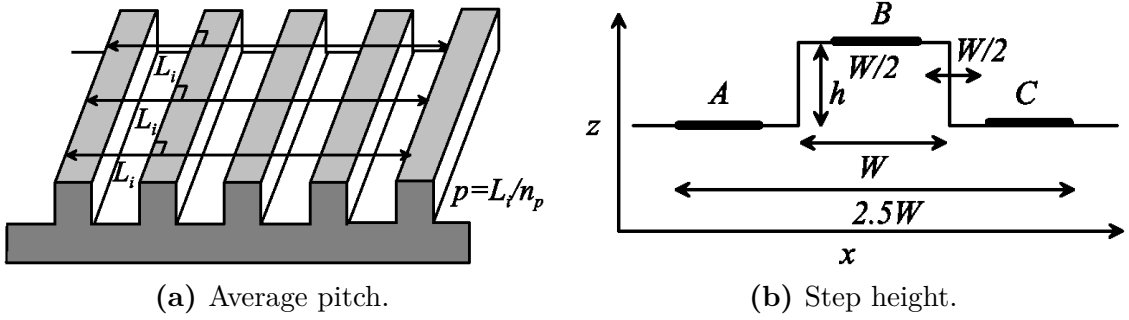


Figure 9. 1D AFM measurement: (average) grating pitch and step height definitions[18].

2.3 MAFM surface measurements

The interferometric scales of an MAFM give measurements direct traceability and thus low uncertainty[17]. One-dimensional features, e.g. grating pitch and step height, have already been measured with uncertainty below 1 nm[18, 19]). These results are achieved by exploiting inherent symmetries in 1D measurements. Fully 3D measurements, however, have been of insufficient precision - a reported figure is 5 nm uncertainty for XYZ-position[4]. This has already been reduced to an acceptable level ($< 1 \text{ nm}$)¹. Traceable 3D measurements with low uncertainty is necessary e.g. for controlling device variability in the semiconductor industry, where node size has shrunk to the nanometer level.

Grating pitch and step height are common 1D features measured by AFM. A 1D grating is a periodic structure of steps and grooves, extending on a single axis, as in fig. 9(a). Pitch measurement of a 1D grating can be done by counting the period of rising edges, or using more advanced algorithm[18, 19]. The measurement is unidirectional, in that only the rising edge is used - if the falling edge is also used, the measurement becomes bi-directional. Periodicity of the structure is used for averaging, and noticeably reduces measurement uncertainty. The same arguments hold for step height measurement (fig. 9(b)). In both cases, the measurand - quantity of interest - can be expressed as a scalar function of several variables.

The current limitations of 3D AFM measurements are outlined by Dixon et al.[20]. One of the limitations is the imaging of almost-vertical features, i.e. steep

¹Private communication with V. Korpelainen, and 3DNano consortium.

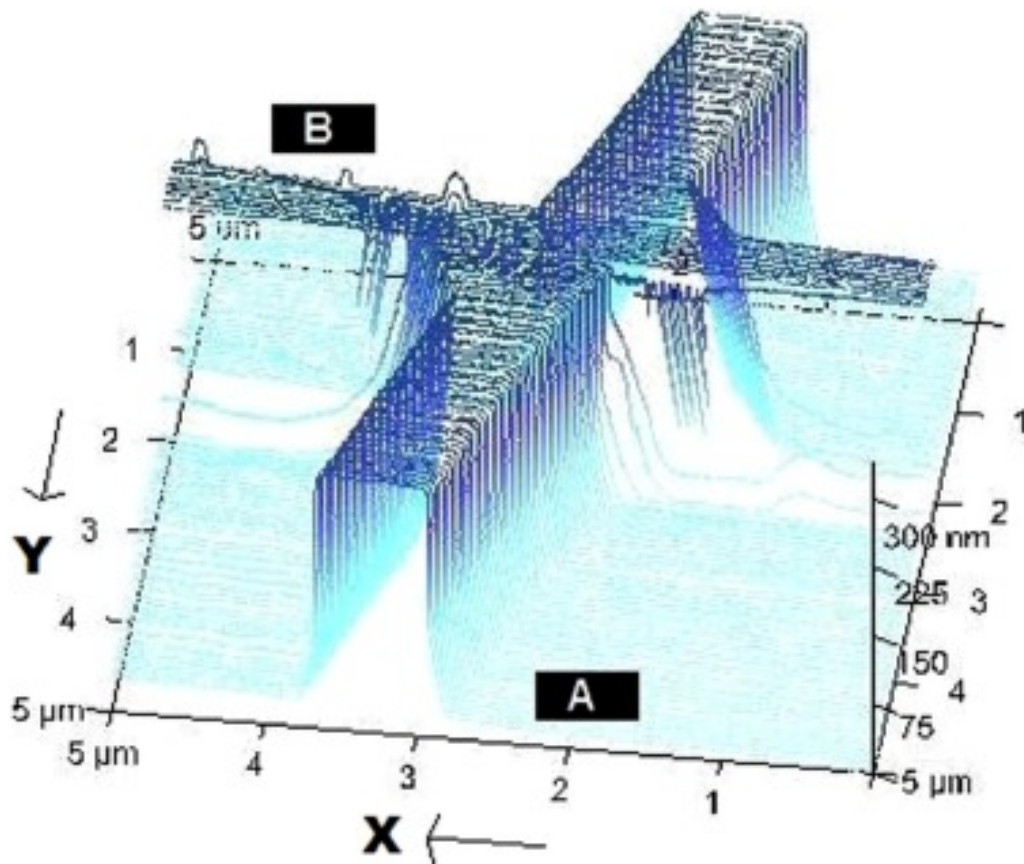


Figure 10. AFM image of two perpendicular raised lines[20]. Sidewalls of line B are not captured, as they lie parallel with the fast scan direction (X).

surface gradients. They are notoriously troublesome to image, which can be seen in fig. 10. In the figure, two perpendicular raised lines are scanned using a typical raster pattern. Where the fast scan direction runs alongside the sidewall of a line, there is insufficient sampling to reconstruct the full wall. By tilting the sample/probe, i.e. touching the surface at an angle, this issue can be partly remedied[21, 22]. However, this introduces sensitivity to scan direction.

3 Expression of uncertainty and Monte Carlo

Monte Carlo (MC) is a family of methods used for generating an output distribution by evaluating a function on randomly sampled input. Techniques for using randomness to determine a value, or a constant, exist from as early as the 17th century. Buffon's needle, attributed to the French scientist Comte de Buffon (1707-1788), was an experimental method for obtaining the value of π . He proved that by repeatedly tossing a needle of length L onto a lined background (with spacing L), he could estimate the ratio $2/\pi$ by the probability of the needle intersecting a line. The same concept is used in modern Monte Carlo, where random number generators are used in lieu of a human operator. What remains common to both Buffon's needle and modern Monte Carlo is the idea of exploring system behavior through randomness.

In this section, a short introduction to a basic Monte Carlo method will be given. This includes the key theories needed for understanding how and why the method generates meaningful output. An important application, the expression of measurement uncertainty, will be explored by reviewing the standard metrological framework.

3.1 Notation

Being of random and thus statistical nature, MC features heavily the notations and concepts from statistics. This subsection briefly presents the key concepts used throughout the entire section, from variables to distributions.

Random variables are typically denoted by capital letters (X), and random vectors are bolded (\mathbf{X}). The probability that a random vector will have a specific value is expressed as $\mathbb{P}(\mathbf{X} = \mathbf{x})$, where $\mathbf{X}, \mathbf{x} \in \mathbb{R}^d$. Typically, a random variable will have an associated probability distribution, i.e. a map of the above probability with

respect to specific values. For a continuous random variable, the associated probability density function (PDF) g and cumulative density function (CDF) G are defined:

$$\begin{aligned} G_X(\varepsilon) &= \mathbb{P}(X \leq \varepsilon), \\ g_X(\varepsilon) &= dG_X(\varepsilon)/d\varepsilon = \mathbb{P}(X = \varepsilon), \\ \int_{-\infty}^{\infty} g_X(\varepsilon)d\varepsilon &= 1 \end{aligned} \tag{3}$$

The most common statistics of a random variable are its expectation value and variance, $\mathbb{E}(X)$ and $\text{Var}(X)$. When handling multiple variables, it is common to also look at their mutual variance, i.e. covariance $\text{Cov}(X,Y)$.

$$\begin{aligned} \mathbb{E}(X) &= \int_{-\infty}^{\infty} g_X(\varepsilon)\varepsilon d\varepsilon, \\ \text{Var}(X) &= \mathbb{E} \left((X - \mathbb{E}(X))^2 \right), \\ \text{Cov}(X_i, X_j) &= \mathbb{E} \left((X_i - \mathbb{E}(X_i))(X_j - \mathbb{E}(X_j)) \right). \end{aligned} \tag{4}$$

Sampling a random variable, i.e. generating a value based on a distribution, can be done using several techniques, most of which are beyond the scope of this thesis. The Guide to expression of Uncertainty in Measurement (GUM)[3] contains recipes for sampling from different distributions using uniformly distributed random numbers $U(a,b)$. Most distributions have a default implementations in Matlab, and any distribution can be replicated using so-called inverse transform sampling. The most common distributions are the uniform and the Gaussian distribution, both of which are extensively used in metrology.

3.2 Standard framework for expressing uncertainty

When measuring some quantity, we have only a best estimate of what its value should be. There is ambiguity surrounding the result, in that reflects both the true value of the quantity and additional effects which we do not know about. It is this “dispersion on values” is what the GUM[1] defines as uncertainty.

To construct uncertainty, we rely either on statistics based on direct observation

(Type A evaluation), or statistics using a priori knowledge of the measurand (Type B evaluation). Either statistics can be used to evaluate a model function, based on the assumed behavior of some system, to produce an output. The GUM framework then provides procedure for composing the uncertainty of inputs to form the uncertainty of output (standard propagation). It is this concept that we shall briefly explore.

Type A evaluation is simple statistics:

$$\begin{aligned}\bar{X} &= \frac{1}{n} \sum_{i=1}^n X_i, \\ s^2(X_i) &= \frac{1}{n-1} \sum_{j=1}^n (X_j - \bar{X})^2, \\ s^2(\bar{X}) &= \frac{s^2(X_i)}{n}.\end{aligned}\tag{5}$$

Here, the experimental mean \bar{X} serves as an estimate for the true expectation value of the random variable. The term $s^2(X_i)$, the experimental standard deviation, is a measure of uncertainty in the arithmetic mean \bar{X} . The standard deviation of the mean, $s^2(\bar{X})$, tells us how closely the arithmetic mean approximates the true expectation value, and is used as the standard error. Type B evaluation, on the other hand, requires some additional information about the measurement, such as previous data or calibrations.

A best estimate for the model output is generated using the experimental means of its variables. The combined uncertainty is determined by the means' standard deviations:

$$\begin{aligned}\tilde{Y} &= f(\bar{X}_1, \dots, \bar{X}_N) \\ u^2(\tilde{Y}) &= \sum_{k=1}^N \left(\frac{\partial f}{\partial X_k} \right)^2 s^2(\bar{X}_k)\end{aligned}\tag{6}$$

If the best estimate now follows either a normal distribution or a t-distribution, a coverage interval and probability can also be obtained. Results can thus be expressed as the interval $Y = \tilde{Y} \pm U$, where U is a multiple of the standard deviation of mean, and a probability that randomly chosen Y falls within this range.

It is apparent now, that calculating measurement uncertainty is an involved procedure, particularly if the number of variables X_k is high or if the partial derivatives

are troublesome to generate. Furthermore, if the output cannot be described by the above-mentioned distributions, the notion of coverage becomes somewhat ambiguous.

3.3 Simple Monte Carlo

Simple Monte Carlo (SMC) is an adequate method when we wish to obtain an estimate without regard to computational time. This subsection will present the simple case of a scalar-valued model function, e.g. a simulation of a single value using multiple inputs. A good overview of this and more advanced methods can be found e.g. in Art Owen's book[23].

Briefly stated, in SMC we evaluate $f : \mathbb{R}^d \rightarrow \mathbb{R}$ using randomly sampled inputs \mathbf{X}_i :

$$\begin{aligned} Y_i &:= f(\mathbf{X}_i), \\ \hat{\mu}_n &:= \frac{1}{n} \sum_{i=1}^n Y_i, \\ s^2 &= \frac{1}{n-1} \sum_{i=1}^n (Y_i - \hat{\mu}_n)^2 \end{aligned} \tag{7}$$

The SMC estimate $\hat{\mu}_n$ is the primary output, and is perfectly unbiased by definition ($\mathbb{E}(\hat{\mu}_n) = \mathbb{E}(Y)$). Variance of the estimate is also unbiased, as $\mathbb{E}(s^2) = \sigma^2$. This procedure is also used in the GUM's guidelines for application of MC[3]. Note that at no point did require that the output's true expectation value (μ) or variance (σ^2) be known.

In an ideal world we would have complete information on the output's distribution, including expectation value and variance. SMC, however, manages to reproduce this information with only partial information:

Theorem 3.1 (*(Weak) Law of large numbers*). *Let Y_1, \dots, Y_n be independent and identically distributed (IID) random variables, with $\mathbb{E}(Y_i) = \mu$. Then, for any choice of $\epsilon > 0$:*

$$\lim_{n \rightarrow \infty} \mathbb{P}(|\hat{\mu}_n - \mu| \leq \epsilon) = 1.$$

In brief, the error in SMC's estimate can be made vanishingly small by increasing

the number of trials (generated outputs).

It can be shown that SMC's estimate is unbiased, i.e. its expectation value is identical to the variable it attempts to reproduce. First, assume an expected value and a finite variance, i.e. $\mathbb{E}(Y) = \mu$ and $\text{Var}(Y) = \sigma^2 < \infty$. Then we can prove the lack of bias, and show how the estimate's error declines when increasing number of trials (n):

$$\begin{aligned}\mathbb{E}(\hat{\mu}_n) &= \frac{1}{n} \sum_{i=1}^n \mathbb{E}(\mathbf{Y}_i) = \mu, \\ \text{Var}(\hat{\mu}_n) &= \mathbb{E}((\hat{\mu}_n - \mu)^2) = \frac{\sigma^2}{n}.\end{aligned}\tag{8}$$

Note that variance of the estimate, i.e. the estimate's error, is unaffected by model dimensionality, complexity and smoothness.

Finally, as a justification for using SMC as a replacement for the standard propagation of uncertainty in measurements[3, 23]:

Theorem 3.2 (*Central limit theorem*). *Let Y_1, \dots, Y_n be independent and identically distributed (IID) random variables with mean $\mathbb{E}(Y_i) = \mu$ and associated finite variance $\sigma^2 > 0$. Let our estimate of the mean be $\hat{\mu}_n = (1/n) \sum_{i=1}^n Y_i$.*

$$\forall z \in \mathbb{R} : \lim_{n \rightarrow \infty} \mathbb{P} \left(\sqrt{n} \frac{\hat{\mu}_n - \mu}{\sigma} \leq z \right) = \Psi(z; 0, 1),$$

where $\Psi(z; 0, 1)$ is the CDF of the normal distribution, with mean 0 and standard deviation 1.

The above tells us that SMC's estimate will have a distribution that tends towards the normal distribution. To be precise, this is a valid argument for any estimate based on arithmetic average, e.g. mean values obtained from repeat measurements.

3.4 Application of Monte Carlo to measurement uncertainty

In order to apply SMC to measurement uncertainty, the following conditions must apply[3]:

1. The model function f is continuous with \mathbf{X} in the neighbourhood of their best estimates (mean values).
2. For output Y , both $\mathbb{E}(Y)$ and $\text{Var}(Y)$ exist.
3. Number of SMC trials (i.e. n in current notation) is sufficiently large.
4. (PDF for output is continuous and strictly increasing).
5. (PDF is continuous where it is strictly positive).
6. (PDF has a single peak, and decreases to when moving to either side of said peak).

The first two are necessary for expressing SMC estimate with standard uncertainty, while the last three are for determining coverage intervals of the estimate.

The VIM[5] defines the term “coverage interval” as “interval containing the set of true quantity values of a measurand with a stated probability, based on the information available”. In other words, the coverage interval associated with a 95% coverage probability is defined by:

Definition 3.1 (*Coverage interval*). For a random variable Y and a best estimate μ , there is a coverage probability of $100p\%$ and a coverage interval $[y_l, y_h]$ such that:

$$\mathbb{P}(\bar{\mu} - \mu \in [y_l, y_h]) = p,$$

where $\bar{\mu}$ is the arithmetic mean, as previously defined.

Example 3.1 (*Coverage by standard propagation, jcgM 100:2008*). a normally distributed random variable $y \in n(0, 1)$ has a 95% coverage probability for the coverage interval $[-1.96\sigma, 1.96\sigma] = [-1.96, 1.96]$. 95% of the area under $n(0, 1)$'s pdf, when centered on 0, lies within this interval.

A standard procedure, which should be taken as canon, exists for generating coverage

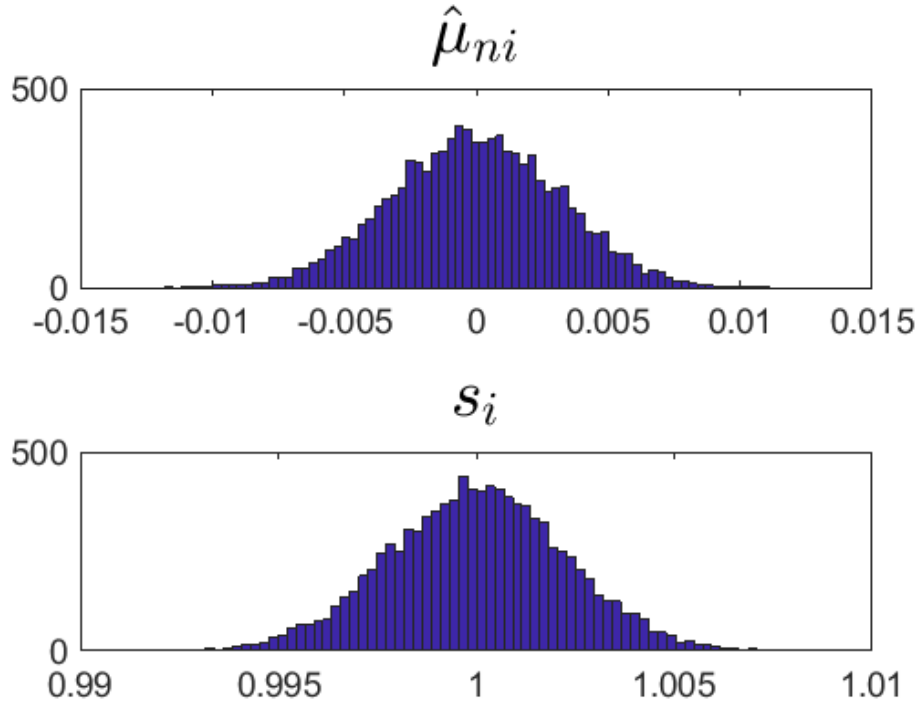


Figure 11. Simple Monte Carlo, estimated parameters of $N(0,1)$ distribution.

intervals within in the context of SMC for measurement uncertainty[3]. In the procedure, unique intervals are identified as pn contiguous items in the set of outputs Y_i , sorted in ascending order. This procedure will be outlined in example 3.3.

Example 3.2 (*Output distribution of SMC*). For a normally distributed random variable $X \in N(0,1)$, we attempt to reproduce it distribution by SMC. We set the number of trials for a single SMC simulation $n = 1 \times 10^5$, and re-run the simulation for a total of $m = 1e4$ times. For a 95% coverage interval to be correct within one or two significant digits, the GUM[3] recommends setting $n > 1 \times 10^6$.

Now, for $i = 1, \dots, m$, generate $X_{1i}, \dots, X_{ni} \in N(0,1)$, and an estimate $\hat{\mu}_{ni}$ and variance s_i^2 using eq. 7. Resulting “experimental” distributions of SMC’s estimate for mean and standard deviation are presented in fig. 11.

In this instance we can see that the distribution is fairly well reproduced, since $\mathbb{E}(\hat{\mu}_{ni}) \approx -5e - 5$ and $\mathbb{E}(s_i) \approx 1$.

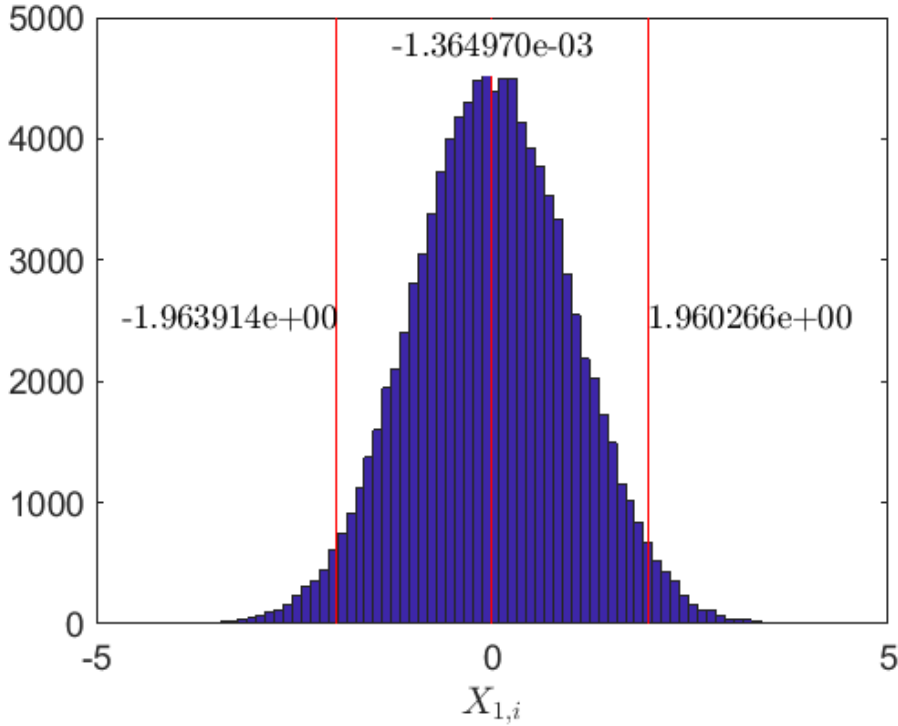


Figure 12. SMC estimate of $X_{1,i} \in N(0, 1)$ with 95% coverage interval.

Example 3.3 (*Coverage by GUM procedure for Monte Carlo*). We now look at a single simulation of example 3.2, i.e. $i = 1$, and determine the estimate's 95% coverage interval. First we set $q = 9.5e5$. Then, we determine the symmetric coverage interval[3].

With $r = (m - q)/2$ we obtain the interval $[X_{1,r}, X_{1,(r+q)}] \approx [-1.964, 1.960]$.

We find that examples 3.1 and 3.3 are in close agreement, and can thus conclude that SMC gives a good approximation to coverage intervals. Looking at the latter example's approximately Gaussian distribution, we can also justify using the central limit theorem.

4 System model and uncertainty

MAFM measurements are affected by potentially hundreds of system parameters, each affect some part of the device. Each part can be separately modeled, and each part contributes to measurement uncertainty. Not all parts contribute equally to uncertainty[2], and thus an initial system model can contain just the largest uncertainty sources. The largest uncertainty sources will be modeled, and used to evaluate standard uncertainty of XYZ-positioning.

Core modules, i.e. significant uncertainty sources, of the system model are shown in fig. 13. Not all modules have been implemented in the scope of this thesis. Some modules' uncertainty contribution depends on position and/or size of measurement (see e.g. [17, tbl. 1]). These will be characterized: Abbe error, orthogonality error (and to a lesser extent laser wavelength and refractive index of air). Also, interferometer mirror surface shape is investigated, but with only qualitative results and no resulting module.

4.1 Abbe error

Ideally, the motion stages of the MIKES MAFM (fig. 7) should provide ideal linear motion. All mechanical devices suffer from motion errors, and these affect also the MIKES MAFM's stages (see fig. 14). Effectively, rotations of the stages (both XY and Z) translate to a rotation of the probe. Abbe's principle[24] tells us that if the axis of readout is not in line with the probe's apex, measurement errors will occur. This subsection will present and characterize the error.

The motion stages can rotate about any of the three principal axis during motion. There are three rotation components about each of the three principal axes. We write $\theta_{x,\alpha}$ for rotation about the x-axis that occur during motion along the α axis.

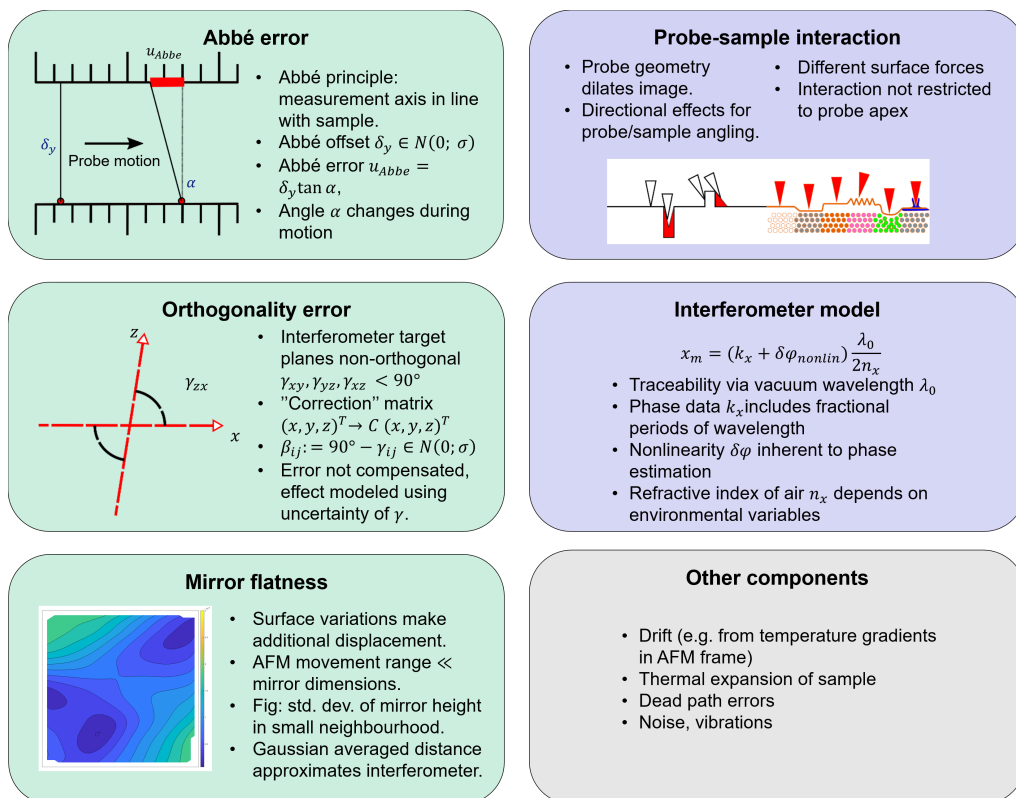


Figure 13. Core modules of MIKES MAFM system model. Left column shows the modules which have been already implemented.

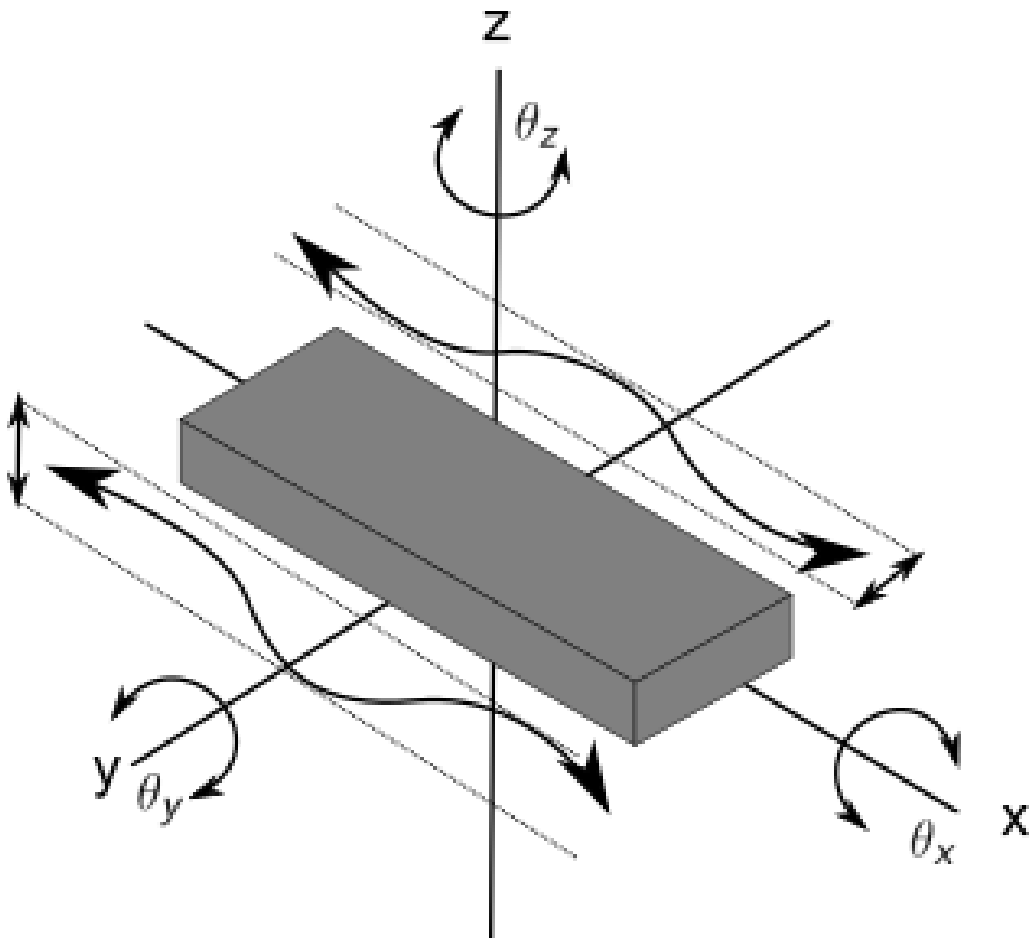
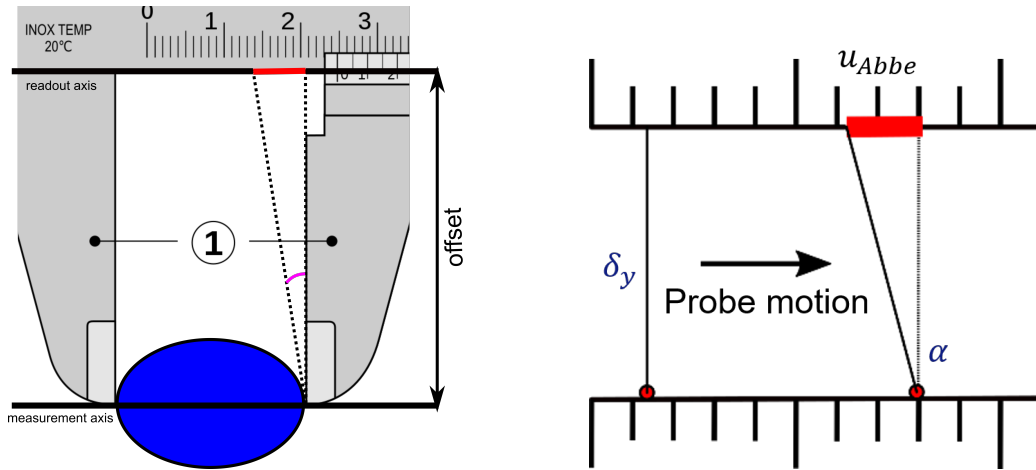


Figure 14. Motion errors of a linear stage, nominally moving on the X-axis. Flatness and straightness errors (wobbly lines) are not labeled: in an MAFM, they are compensated by feedback from interferometers.



(a) The Abbe error (red line) associated with (b) Abbe errors of an AFM, from Abbe offset a rotation (purple arc) of a caliper's jaws. δ_y and probe/sample rotation α .

Figure 15. Abbe errors

Sequential rotations can be described as a matrix (see e.g. R. P. Paul's textbook on robotics[25]). For very small angles, the corresponding linear approximation of this matrix is:

$$\mathbf{R} = \begin{bmatrix} 1 & -\theta_{z,\alpha} & \theta_{y,\alpha} \\ \theta_{z,\alpha} & 1 & -\theta_{x,\alpha} \\ -\theta_{y,\alpha} & \theta_{x,\alpha} & 1 \end{bmatrix} \quad (9)$$

The effect of a rotated probe is best illustrated by an example, fig. 15(a), which shows a round object being measured in the jaws of a caliper. According to the revised Abbe's principle[26], readout error is minimized by having the measurement axis (where object's width is measured) and effective readout axis (caliper scale) lie along the same line. In the figure, the two axes run parallel, but at an offset - an Abbe offset - which results in a readout error that depends on jaw rotation/bending. The Abbe error is a function of offset (a) and rotation (θ):

$$u_{\text{Abbe}} = a \tan(\theta) \approx a\theta \quad (10)$$

Each of interferometer represents a readout axis, and is offset on the two other

axes (e.g. x-interferometer has offsets $a_{x,z}$ and $a_{x,y}$). The Abbe error then becomes:

$$\vec{u}_{\text{Abbe},\alpha} = \begin{pmatrix} a_{x,z}\theta_{y,\alpha} + a_{x,y}\theta_{z,\alpha} \\ a_{y,x}\theta_{z,\alpha} + a_{y,z}\theta_{x,\alpha} \\ a_{x,z}\theta_{x,\alpha} + a_{z,x}\theta_{y,\alpha} \end{pmatrix} \quad (11)$$

where e.g. $\theta_{x,\alpha}$ denotes rotation about the x -axis for motion along the α -axis.

Reducing the Abbe offsets to zero would in theory eliminate the errors, but this is impossible in practice. Lasers have a finite spot size, and the determination of an ‘axis’ within the spot is bound to contain an uncertainty. Spot size cannot be shrunk without introducing diffraction effects or increased optical sensitivity[27]. In addition, the MIKES MAFM’s interferometers (fig. 7) have two beams, separated by an offset. Thus, the ‘axis’ is purely virtual, and is located midway between the beams.

4.1.1 Rotations of the XY-stage

The horizontal / vertical angles of the plane mirrors was measured during motion on X, Y and Z axes. The orientation of a virtual mirror cube, shown in fig. 16, is expressed as a function of the rotations in eq. 9. Analytic expression for orientation is obtained using Matlab’s symbolic toolkit. In a first-order approximation, orientation is the same as rotation angle θ . We can thus directly measure the angles $\theta_x, \theta_y, \theta_z$, and construct a model for Abbe error (eq. 11).

The electronic autocollimator, Möller-Wedel Elcomat 3000, is capable of simultaneously measuring the horizontal and vertical angles of a plane mirror (see fig. 17). Measurement of the X-mirror (next to ‘MEAS’ beam pointing along X axis in 7), is used to determine θ_y and θ_z for the XY-stage. The stage goes through linear motion on either X or Y axis, and the autocollimator is read at set locations. This yields two profiles, whose heights correspond to either θ_y and θ_z . Profile for θ_x is obtained by repeating the measurement using now the Y-mirror.

A number of scan paths were generated, alternative in step size, length, and axis (either X or Y). The plan was to obtain information regarding repeatability,

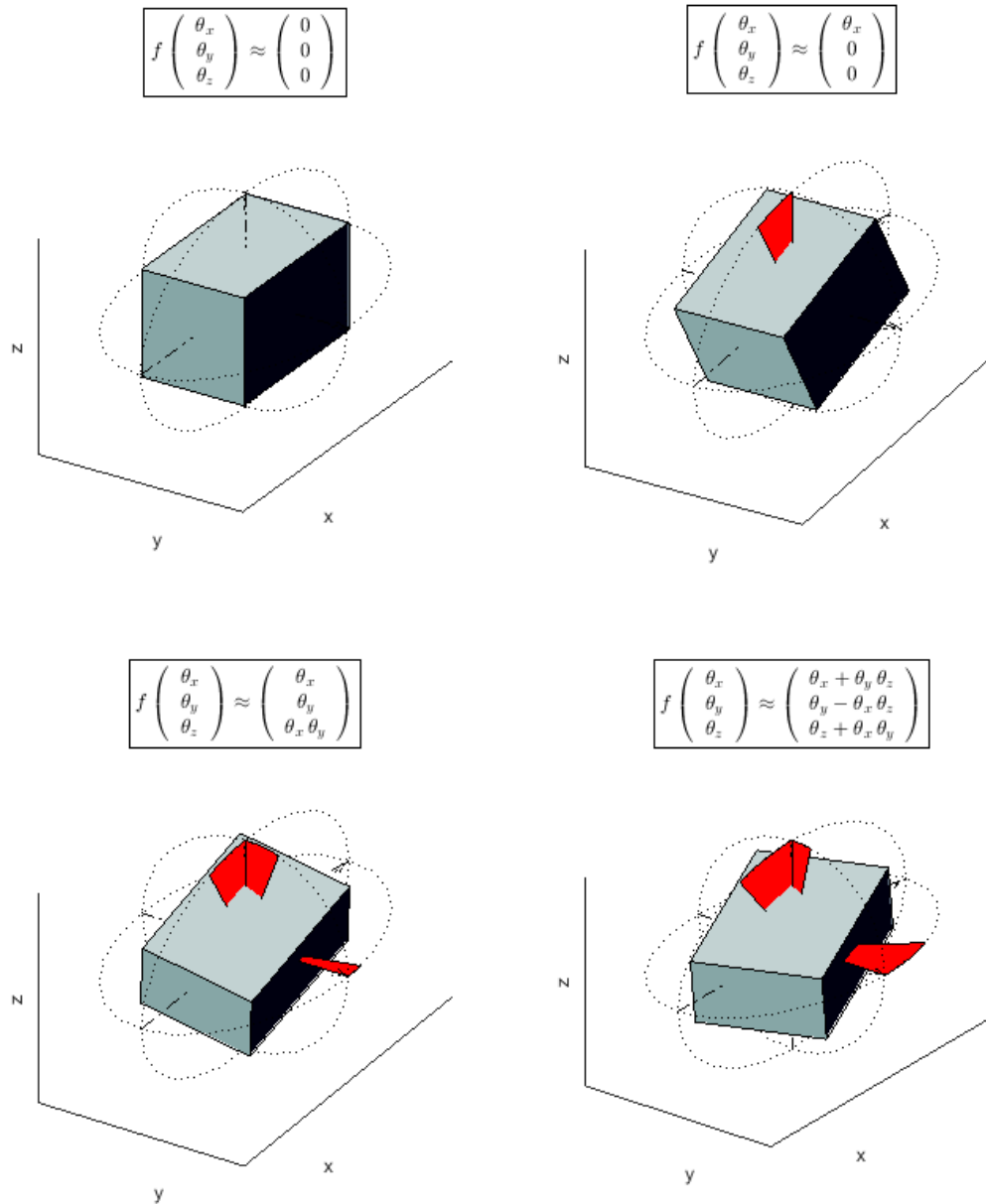


Figure 16. Rotated mirror cube, and the orientation of its faces. Rotations are sequential, and in a local (and previously rotated) coordinate frame. Orientation is represented by a vector function $f(\dots)$, whose magnitude is shown by filled red arcs.

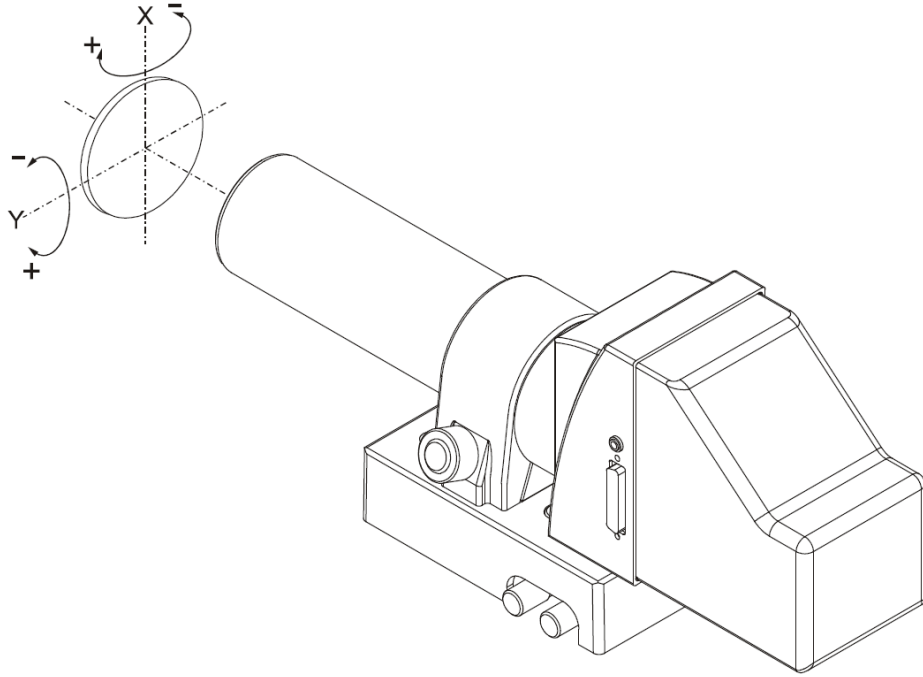


Figure 17. Electronic autocollimator, type Möller-Wedel Elcomat 3000. Can simultaneously measure two angles of rotation of a plane mirror target.

directionality and overall magnitude of the rotation angles. Closed-loop operation was selected for the XY-stage, i.e. a feedback loop using internal capacitive sensors is used for positioning. Noise of the stage's internal sensor is significant, and imposes a practical limit of 25 nm on the minimum step size. However, in the actual MIKES MAFM setup, interferometers provide sensor data for positioning. Thus, the minimum step size is applicable only to the present measurements.

Measurements were timed to start after office hours to minimize disturbances, and would last for approximately 14 h. In both X-mirror and Y-mirror measurement, there was noticeable drift of the horizontal angle (i.e. $\theta_{z,x}$ and $\theta_{z,y}$). An attempt to remedy this was done by zeroing the angles of each linear scan individually, i.e. subtracting the first value of θ . This is justifiable, since Abbe errors are affected only by the **change** in rotation. The result is shown in fig. 18.

After zeroing the data, we compare the horizontal angles of motion on a single axis, measured off both X and Y mirror. Referring to figs. 14 and 16, we see that

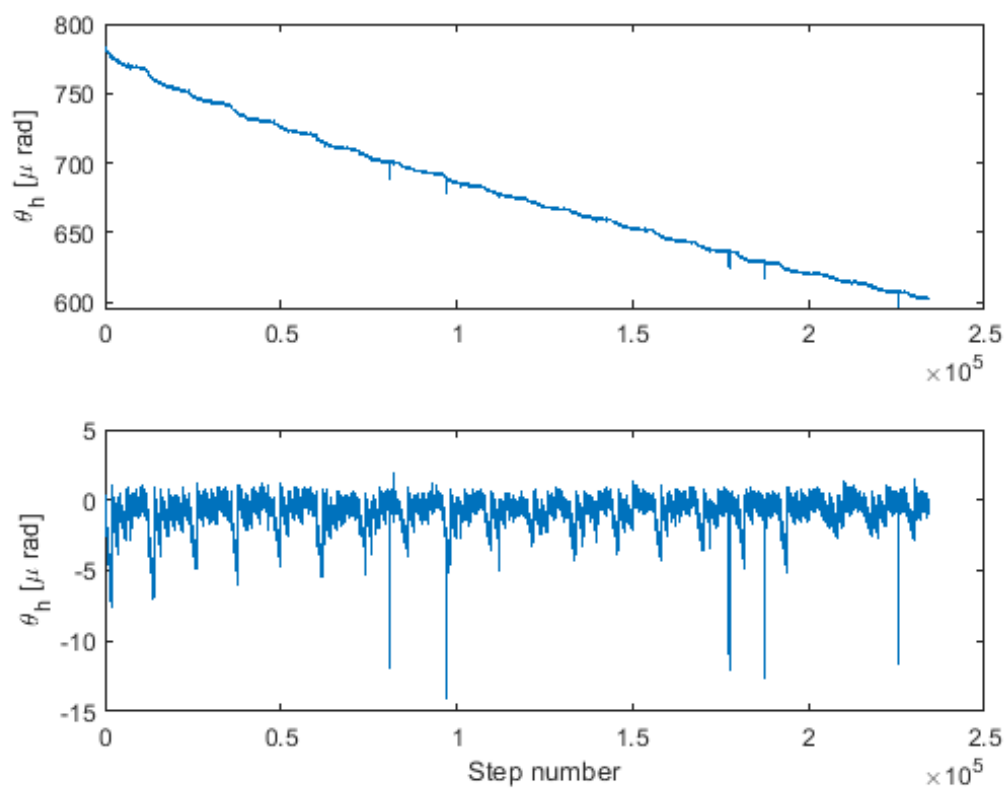


Figure 18. Horizontal angle during alternating X and Y motion of the XY-stage, over a duration of approx. 14 h. Top: data with drift. Bottom: each scan is zeroed.

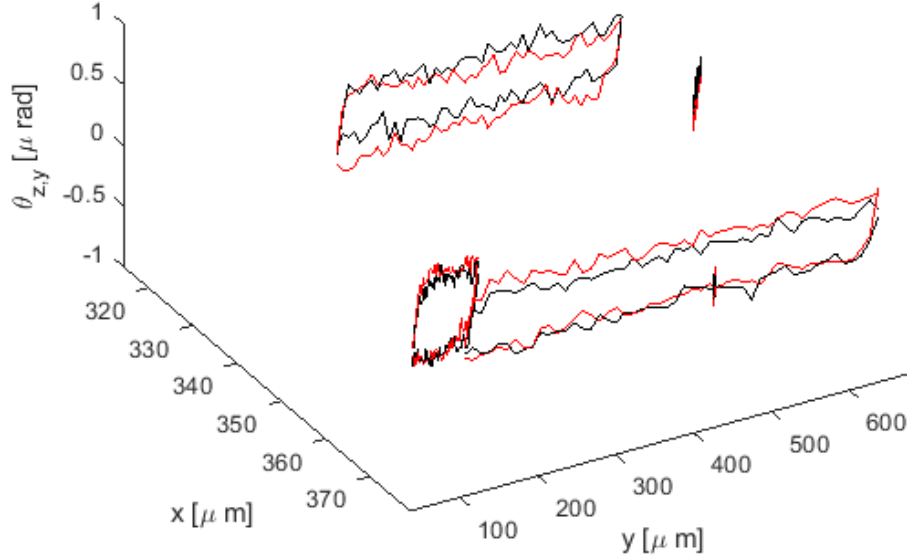


Figure 19. Linear scans along Y axis, nominally identical angle, with directional effect (different values depending on motion direction). Red: i.e. X-mirror measurement. Black: Y-mirror measurement.

horizontal rotation should be identical for both mirrors:

$$\theta_h = \theta_{z,\alpha}, \alpha = x,y \quad (12)$$

Partial data-sets for X-axis scans using either mirror are shown for comparison in fig. 19. Several things are evident from the figure:

1. Data is directional: each ‘loop’ is formed by the trace and retrace (positive and negative direction) of a single linear scan.
2. The initial rise/descent length from a loop’s edge appears independent of scan length or position.
3. The nominally identical horizontal angles do in fact appear identical.

For each motion axis (X or Y), linear scans were measured at various positions, and different motion ranges. Each scan consists of trace and retrace, repeated several times. Data at each fixed location is averaged, yielding a single curve to describe

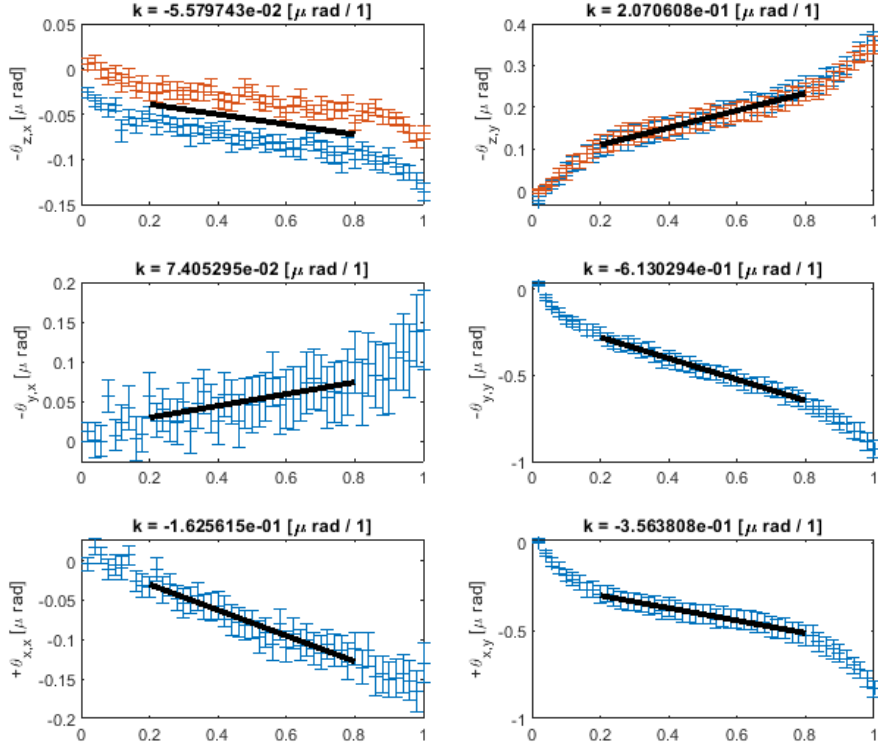


Figure 20. Linearization of rotational errors during motion of the XY-stage, for linear scans of width $\in (0, 100)\mu\text{m}$. Top-left graph shows two nominally identical plots for $-\theta_{z,x}$, whose average is used for the linear fit.

rotation. Averaged data is then normalized, such that the motion range is $(0, 1)$ for every scan, and then binned according to original range. Within each bin, data is again averaged, and fitted to a linear model. The results (two bins) are shown in figs. 20 and 21. 20% of the range was cut from either end before fitting.

As a result of the above procedure, rotations of the XY-stage during XY-motion can be expressed using two linear models. Each model is representative of a motion range, e.g. scan width of $100\mu\text{m}$ to $800\mu\text{m}$. In both cases, total rotation becomes the sum of two linear parts:

$$\theta_\beta = \frac{x - 400}{\Delta x} k_{\beta,x} + \frac{y - 400}{\Delta y} k_{\beta,y}, \quad (13)$$

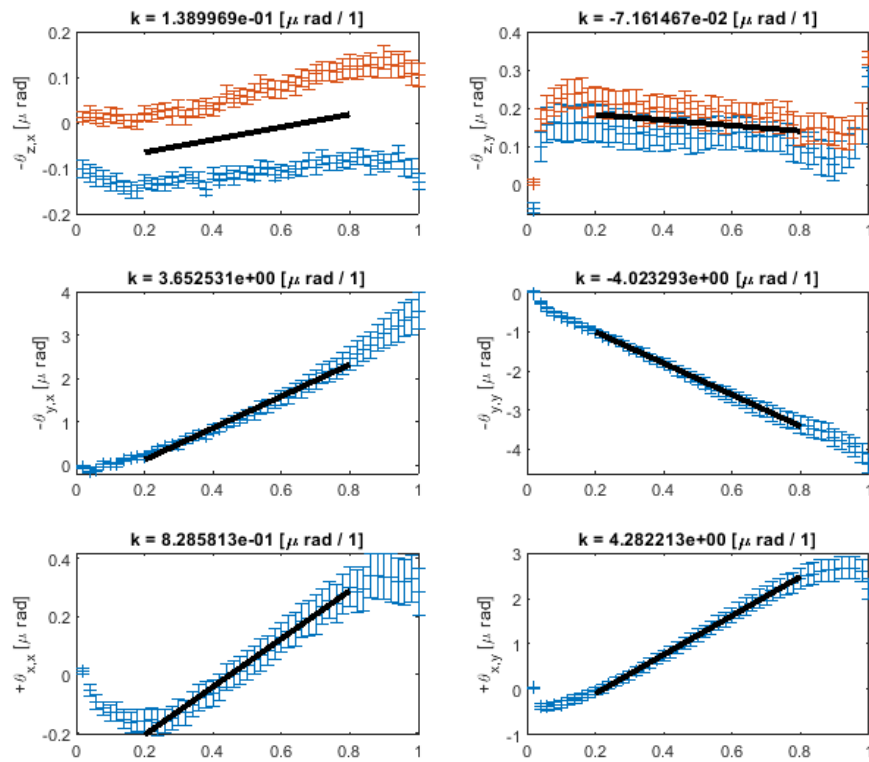


Figure 21. Linearization of rotational errors during motion of the XY-stage, for linear scans of width $\in (100, 800)\mu\text{m}$. Top-left graph shows two nominally identical plots for $-\theta_{z,x}$, whose average is used for the linear fit.

where θ_β denotes total rotation about β -axis, and $k_{\beta,x}$ the slope of linearized $\theta_{\beta,x}$. The parameters Δx and Δy denote length of the motion along either X or Y axis. A value of $400\ \mu\text{m}$ is subtracted such that the rotations are at minimum in the middle of the XY-stage's motion range (at $400\ \mu\text{m}$). If the length of motion is less than $100\ \mu\text{m}$, i.e. $\Delta\alpha < 100\ \mu\text{m}$, then the slopes from fig. 20 are used in eq. 13. Otherwise, slopes from fig. 21 are used.

Summarizing, the rotations of the XY-stage are expressed as linear functions, whose slopes are determined by the length of the motion along X and Y axes.

4.1.2 Rotations of the Z-stage

Open-loop mode was used for Z-motion: the input is a control voltage from the piezo controller, and no sensor reference is available for physical position. This typically introduces non-linearity to the scale as well as hysteresis[28]. Thus, measurement of the Z-stage's rotations were mostly qualitative, and could not yield more than an initial model. However, once the Z-scale is calibrated or sensor reference becomes available, the same methodology can be applied as with the XY-stage.

Several linear scans were created, with different ranges of output voltage at different offsets. Each scan includes sequential trace (motion in positive Z-direction) and retrace (negative direction), repeated a number of times. The same scan paths were used to measure both of the mutually orthogonal mirrors mounted to the Z-stage. Mounting is that of fig. 7, where the mirrors are in the vertical plane, and are marked 'REF'. Total duration for measurements using a single mirror was approximately 30 min.

Like with the XY-stage, there is noticeable directionality of the data. This is evident in the full Z-range scan, fig. 22). Shown is superimposed two separate measurements using the same scan path, but a different plane mirror. The difference between nominally identical angles $\theta_{z,z}$ appears to increase with voltage.

Data for each scan is averaged for both trace and retrace. In addition, the initial trace is removed from each data-set. All data is shown in fig. 23, with different

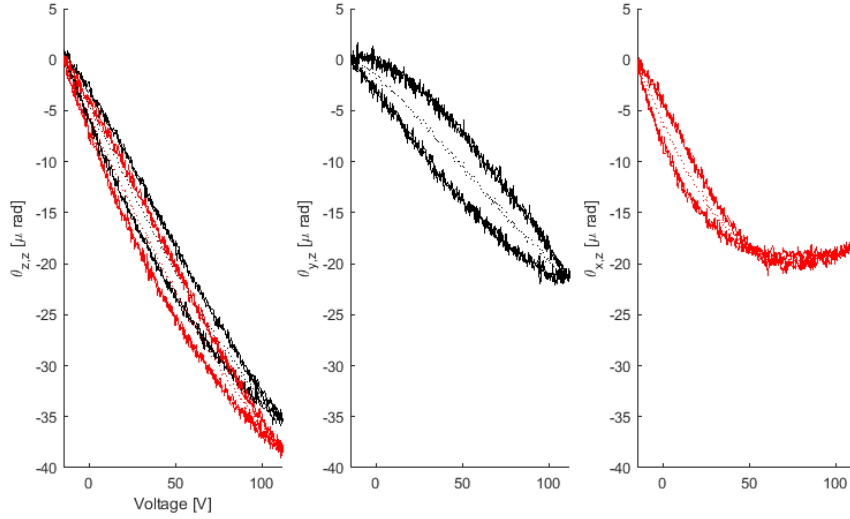


Figure 22. Rotations of Z-stage during Z-motion, initial trace removed, no averaging. Black and red colors denote autocollimator measurements on mutually orthogonal plane mirrors.

colors denoting scans of different voltage ranges. The first column shows $\theta_{z,z}$, i.e. the horizontal angle, which appear to be identical for measurement of the X- and Y-mirrors. The rotations also appear linear with respect to voltage, except for $\theta_{x,z}$. A linearization similar to the one described in subsection 4.1.1 could be constructed, with slope that depends only on voltage range. However, a separate, perhaps piece-wise linear model, should be used for $\theta_{x,z}$.

Since actual position of the Z-stage could not be determined in open-loop mode, the corresponding rotation model was not implemented.

4.2 Interferometer non-orthogonality

The interferometer axes of the MIKES MAFM are not exactly orthogonal to each other, and thus the readout position is in non-Cartesian coordinates. With the Cartesian reference frame centered on the sample origin, the X-interferometer would read a mix of the position along both X, Y and the Z reference axes. One needs a total of six angles to comprehensively relate the Cartesian frame to the non-orthogonal interferometric coordinates. This relation can be described as a six-

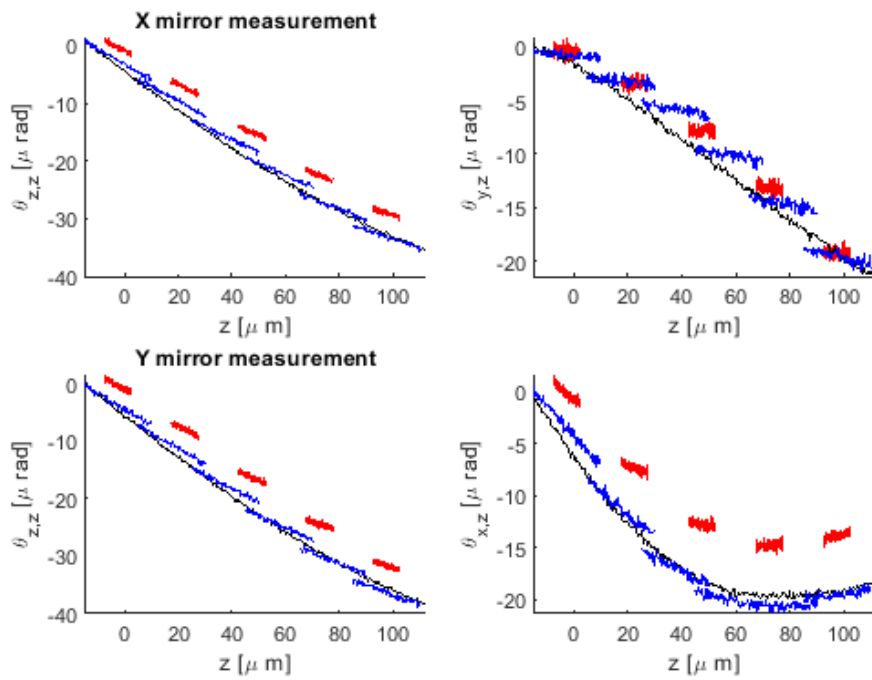


Figure 23. Rotations of the Z-stage during motion. Smaller scan ranges (red, blue) display high linearity.

component correction matrix. In practice, by imposing additional constraints during measurement of angles between interferometric axes, only three angles are needed to construct the matrix. The matrix's exact form varies[17, 29], as does the measurement procedure.

Consider the setup of fig. 24, depicting an Cartesian reference frame (marked x_{ko}, \dots), and a non-orthogonal frame (marked x_k, \dots). The x_{ko} -axis is assumed perfectly aligned with the reference axis x_k , y_{ko} lies in the $x_{ko}y_{ko}$ -plane, and z_{ko} is not constrained in any way. The relation between a point in the Cartesian frame \vec{r} and a point in the non-orthogonal frame \vec{r}_m is:

$$\vec{r}_m = C\vec{r} \quad (14)$$

Where C is the orthogonality correction matrix, which for very small angles can be approximated[17, 29] as:

$$C = \begin{bmatrix} 0 & 0 & 0 \\ \phi_{xy} & 0 & 0 \\ \phi_{xz} & \phi_{yz} & 0 \end{bmatrix} \quad (15)$$

4.3 Mirror flatness

The plane mirrors used as interferometer targets have been glued to a base and mounted to the frame (see fig. 7). This may cause warping of the nominally flat surface, which already has some roughness as per manufacturing specifications. During motion of the MIKES MAFM's stages, the interferometer beams' position on the mirrors will change. Referring to fig. 8, the mirrors are part of the device's metrology loop. As such, interferometers are 'blind' to variations in mirror surface height. These variations should thus be at least qualitatively analyzed.

Surface of the eight mirror targets is measured using a Fizeau interferometer, and obtained as a heightmap Z . The raw heightmap for one of the Z-interferometer mirrors is shown in fig. 25. Since we're basically working with an image, we can use several techniques from image processing[30]. The image (heightmap, Z-data) is processed as follows:

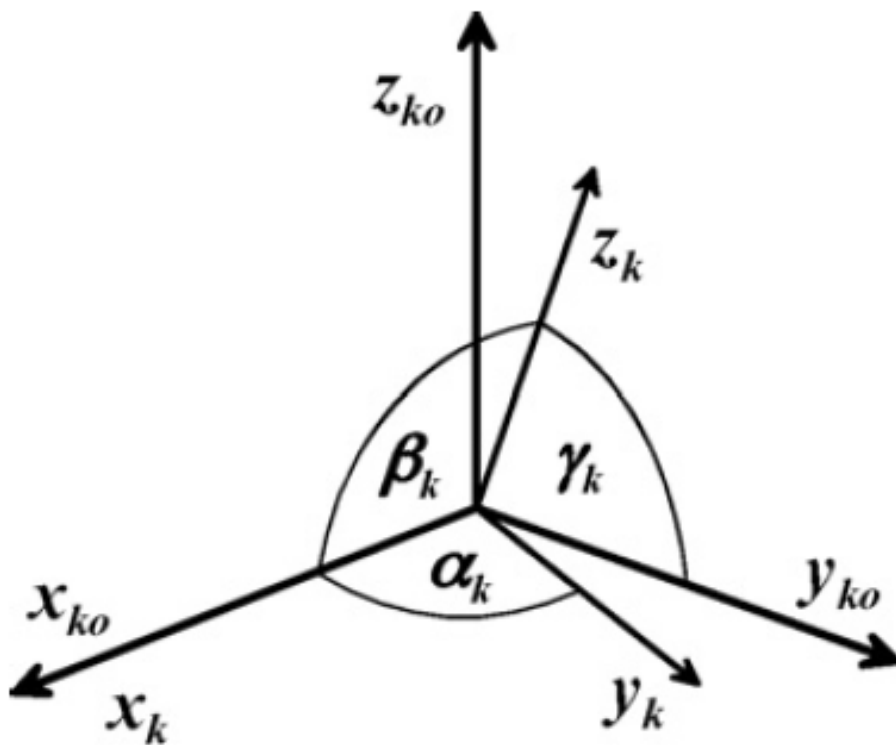


Figure 24. Non-orthogonality of sensor axes[29]. Sensor X-axis x_k is already in line with the actual X-axis x_{ko} , while y_k lies in the x_{ko} - y_{ko} plane.

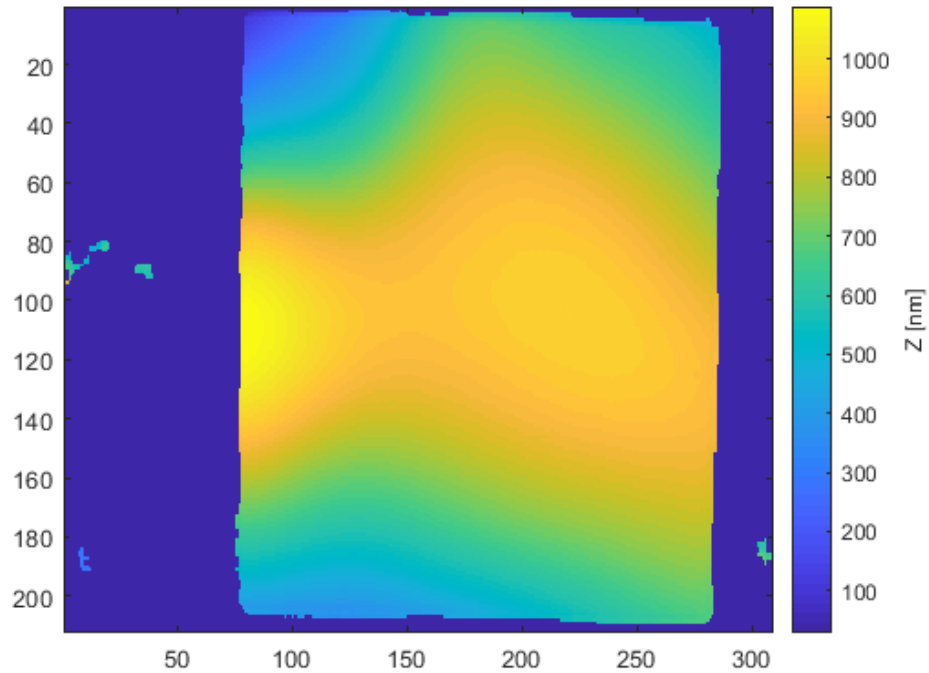


Figure 25. Raw heightmap data for one of the MIKES MAFM’s Z-interferometer mirrors. XY-scales are not calibrated, mirror is not well aligned, and the image is speckled with junk.

1. ‘Specks’ are removed by remove all but the largest connected neighborhood from the image
2. Rotation of mirror is removed using an oriented minimum bounding box algorithm[31]
3. The image is centered and scaled, yielding both X, Y and Z data
4. Z data is smoothed using 2D convolution with a Gaussian kernel ($\sigma = 0.75 \text{ mm}$)

The first three processes serve to clean up the data, and to express it in a standard format. Smoothing reflects the finite spot size of interferometer laser, in a Gaussian beam model. The processed data is shown in fig. 26.

We define flatness as the difference between maximum and minimum height of a surface in a neighborhood. For the MIKES MAFM’s mirrors, this neighborhood is defined by the range of motion of its stages. For example, the full motion range of the XY-stage is a square with side length of $800 \mu\text{m}$. Each Z-interferometer beam

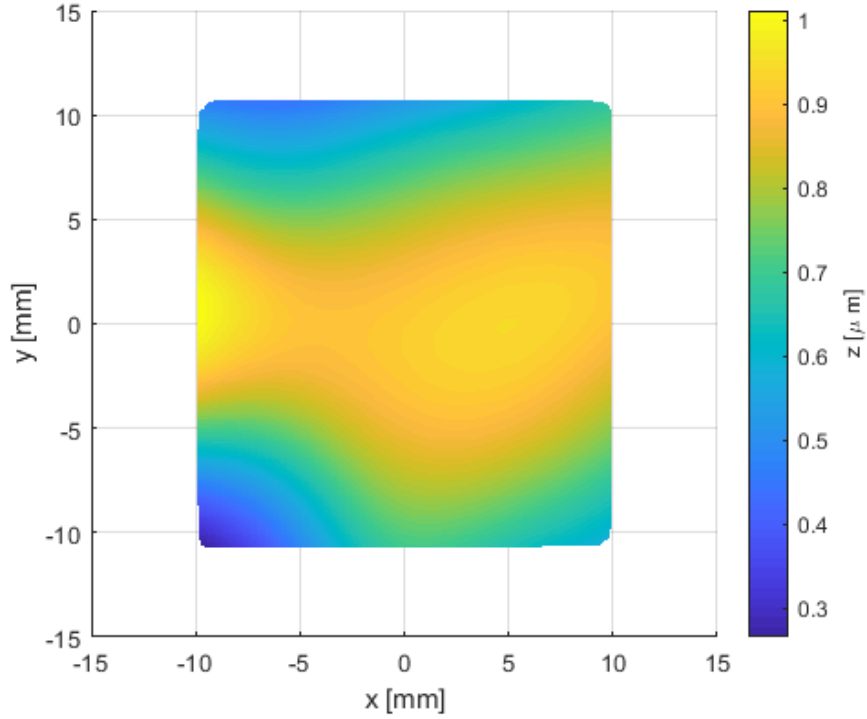


Figure 26. Processed heightmap data for the mirror of fig.25.

axes is then restricted to a square of this size, rather than the full mirror surface.

To determine flatness inside a square area centered on point (x,y) , we use a bit of mathematical morphology[30]. Dilation (\oplus) and erosion (\ominus) are operations by which both the maximum and minimum heights in a neighborhood can be obtain. We now create a suitable mask M , representative of the motion range (800 μm or 100 μm side square, for Z or XY mirrors). Then, we obtain flatness in a moving neighborhood over the mirror's surface:

$$\text{Flat}(x,y)_M = (Z \oplus M) - (Z \ominus M) \quad (16)$$

i.e. we re-define flatness as a localized (x,y) value, that represents the worst-case flatness in the allowed motion range. Flatness of a single Z-mirror is shown in fig. 27.

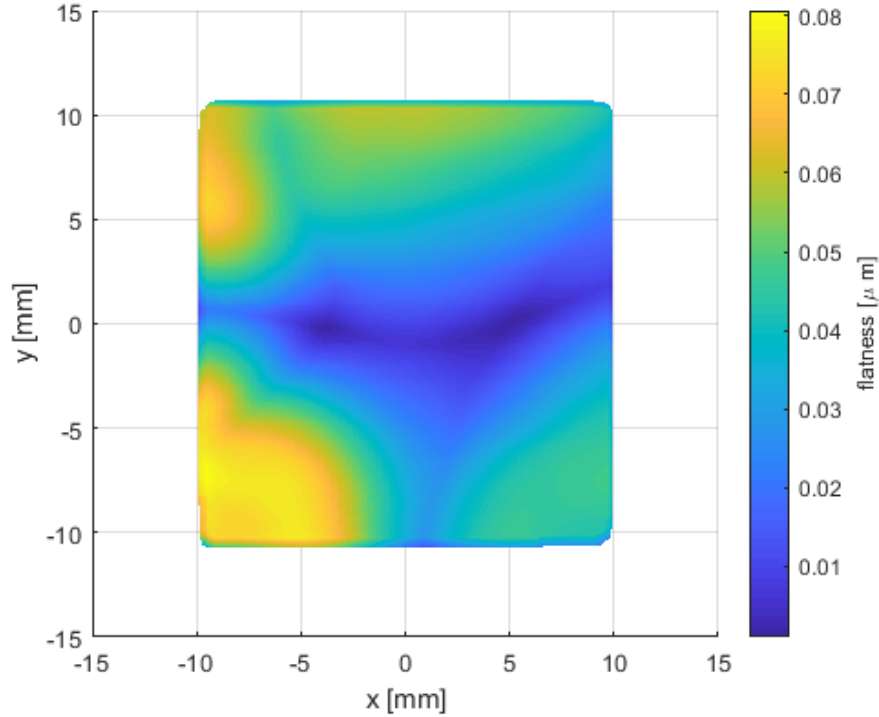


Figure 27. Worst-case flatness in a neighborhood of the Z-mirror.

4.4 Monte Carlo uncertainty evaluation

Simple Monte Carlo (SMC, sec. 3.3) is used to express uncertainty of measurement. The models constructed in previous sections are evaluated initially using synthetic data. A parametric 2D grating, as in fig. 28, is created with freely controllable parameters and rotation. The XYZ-points of the grating's surface were used as position input to the system model.

Abbe errors and orthogonality errors were combined in a single model function:

$$\vec{R}_m(\vec{r}) = \vec{U}_{\text{Abbe}}(\vec{\theta}(\vec{r})) + C\vec{r} \quad (17)$$

where capital letters are used for \vec{R}_m , \vec{U}_{Abbe} and C to denote that they are random numbers. When evaluated, the model yields distributions of XYZ-values at each location \vec{r} . From these distributions, the XYZ positioning errors - standard uncertainties - can be calculated using 7.

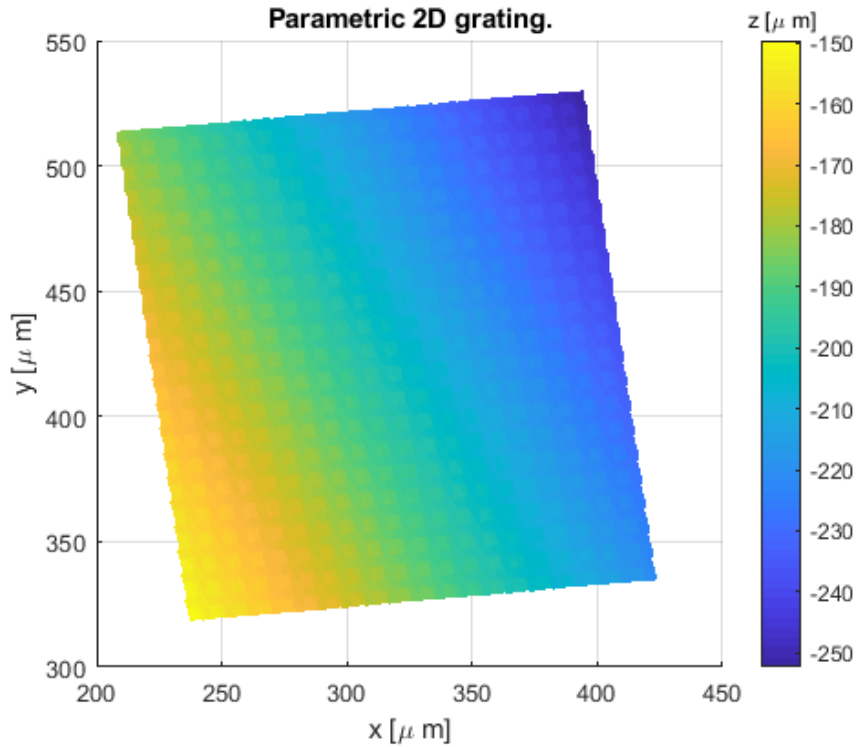


Figure 28. Parametric 2D grating created for evaluating the numerical model.

The number of Monte Carlo trials should be set to 1×10^6 - a number which should be sufficient for uncertainty estimation, according to GUM[3]. However, the synthetic data-set of fig. 28 consists of $512 \times 512 \times 3$ double-precision values (doubles). To store the full output of eq. 17, one would need yet another $512 \times 512 \times 3$ doubles per Monte Carlo trial. As each double requires 8 bytes of memory, total memory needed just for the output is approximately 800 GB.

A representative number of trials, 1×10^5 , was selected as a trial. To overcome memory limitations, only a part of the trials - a chunk - were computed at a time. Also, rather than storing full output distributions, only the uncertainty components were kept. The standard uncertainty for each XYZ-point was then updated after computing each chunk using a single-pass algorithm[32].

Standard uncertainty in positioning, using 1×10^5 Monte Carlo trials, are shown in figs. 29,30 and 31. Uncertainty is position-dependent, as is expected from eqs. 13 and 14. Also, uncertainty in X-position is an order of magnitude lower, likely because the assumptions made in construction of orthogonality correction. Z-uncertainty is

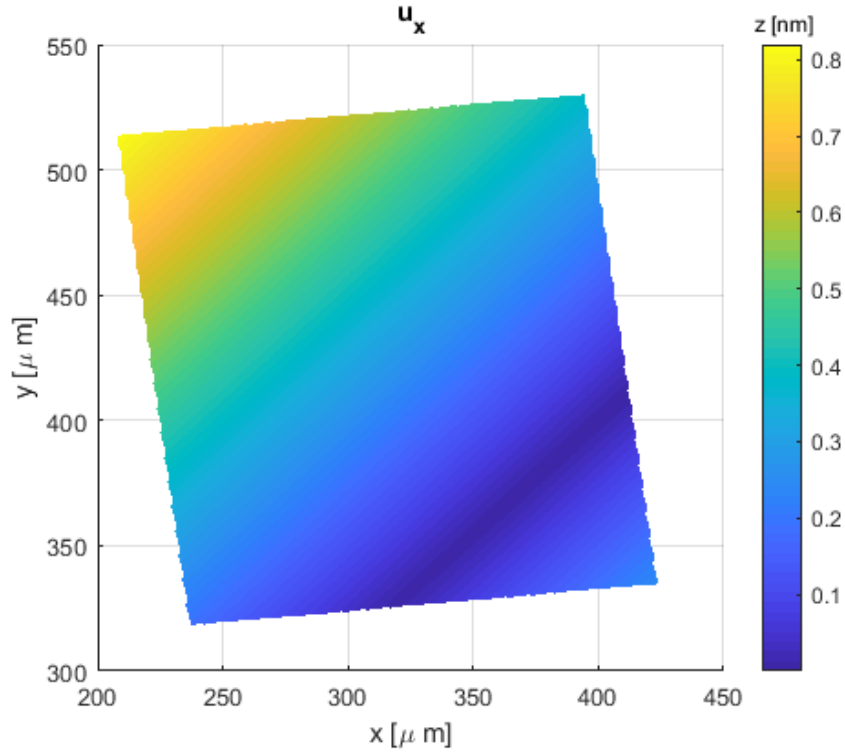


Figure 29. Standard uncertainty of X-position, using simple Monte Carlo with $N = 1 \times 10^5$.

at a minimum near the position $(x,y) = (400, 400) \mu\text{m}$, as this was chosen as origo in the model.

The evaluation of eq. 17 yields the standard uncertainty for an XYZ-point. In practice, however, a quantity of interest - a measurand - is to be computed. An example measurand is grating pitch - the period of steps in fig. 28, in either direction. A model for pitch, i.e. a mapping of the grating surface to a representative value, would then be constructed. Standard uncertainty for pitch would be obtained from the distribution of pitch:

$$P = P(\vec{R}_m(\vec{r}_0), \dots, \vec{R}_m(\vec{r}_N)) \quad (18)$$

where \vec{r}_i represent discrete XYZ points on grating surface. The actual form of the pitch model is omitted, as it is beyond the scope of this thesis.

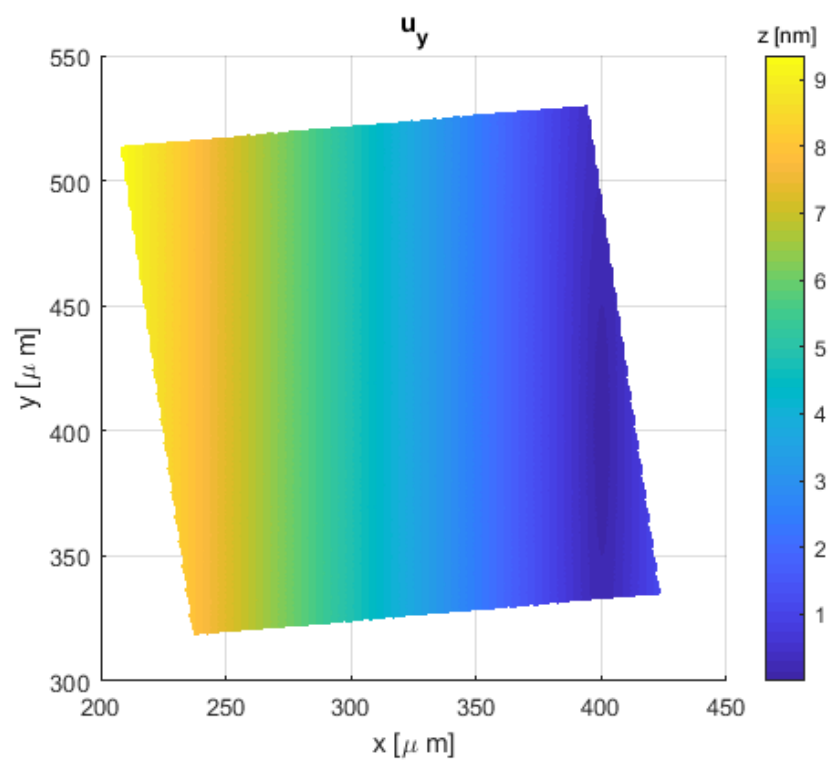


Figure 30. Standard uncertainty of Y-position, using simple Monte Carlo with $N = 1 \times 10^5$.

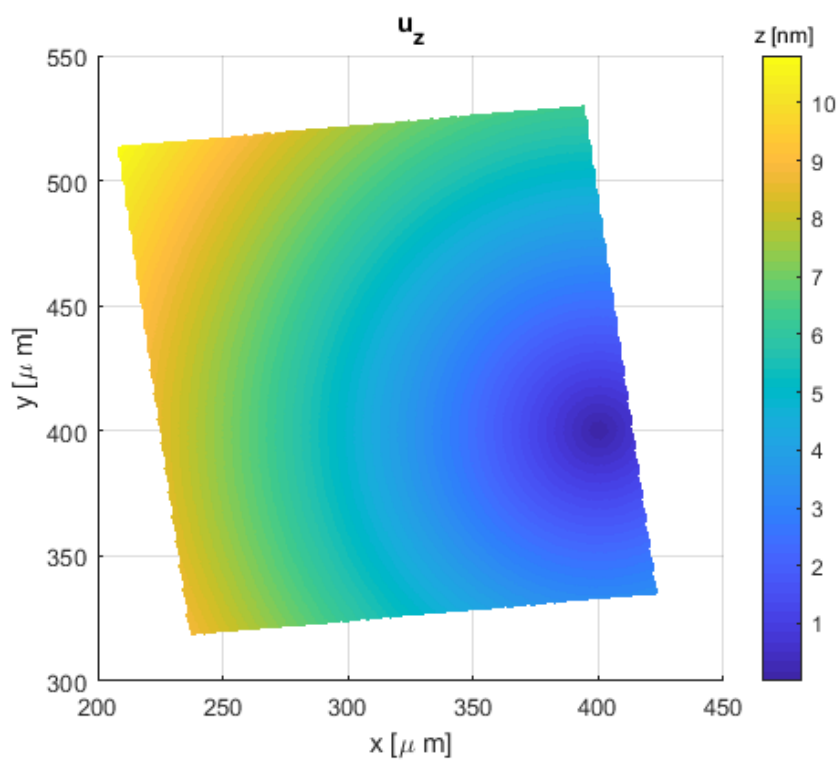


Figure 31. Standard uncertainty of Z-position, using simple Monte Carlo with $N = 1 \times 10^5$.

5 Discussion

The work presented in this thesis consisted of characterizing and then modeling uncertainty source of the MIKES MAFM. We'll now take another look at the results, and their significance. Some assumptions used during data analysis will be revisited. Also, the exclusion of certain modules (system model parts) will be explained.

The motion-induced rotations of the MIKES MAFM's stages were characterized. Long measurement times were required to obtain representative data. A single measurement set, consisting of several long- and short-range motions, lasted approximately 14 h. During this time, one data component (rotation angle) drifted noticeably. The XY-stage was detached from the frame during measurement, and the temporary attachments are the likely cause of drift. Thus, this drift is not representative of the final setup (with stage attached to frame). Drift was compensated for by zeroing each part of the measurement, i.e. having each motion's angles start at zero. With suitable normalization of data, binned according to range of motion, a seemingly linear region in the rotations was detected. Slope of the linear region was then used to parametrize a model for position-dependent rotations.

Non-orthogonality of the interferometer mirrors was also modeled. Angles between the mirror normals are not square, and thus a correction is needed to the measured coordinates. Reference values of the correct order of magnitude were used in place measured angles. As the reference values represents very small deviations from orthogonality, also the correction term could be linearized.

Flatness of interferometer target mirrors was investigated, but not included in the uncertainty model. The flatness was computed in a moving window, representative of the XY- and Z-stages' motion ranges. This procedure can at least give a qualitative view of worst-case flatness for a given alignment of the interferometers. As the mirrors are part of the MIKES MAFM's metrology loop, surface variations cannot be

detected, and should thus be included in the system model as a source of uncertainty. However, the mirror data's lateral scales were uncalibrated, and had to be re-sized to nominal dimensions listed in specifications. Because of this, care should be taken in constructing the model.

The constructed system model was evaluated on a generated parametric 2D lattice. Stage rotation model was based on real data, but Abbe offsets and non-orthogonality were taken as representative values (but correct order of magnitude). Standard uncertainty on the lattice's surface was estimated using simple Monte Carlo, with $N = 1 \times 10^5$ trials. The estimate yielded values on the order of nm throughout

The estimated uncertainty is in the nm range for all components. In addition, the X-component is an order of magnitude lower than the others. This is indicative of the orthogonality correction, which does not add variation to the X-component.

Uncertainty for a real measurement was not yet considered, nor was a measurement function constructed. A first step towards real-world use would be to construct a measurement function or model, e.g. of 1D lattice pitch. One would then simply apply the measurement model to the generated distribution of XYZ-data. The measurement model, evaluated with the XYZ-data, should then yield the standard uncertainty of measurement.

6 Conclusions

The MIKES MAFM is a Metrological Atomic Force Microscope intended for traceable 3D nanoscale surface measurements. Traceability was explored in depth, explaining how it stems from the use of interferometric positioning. This thesis also dealt with characterizing the device's uncertainty sources, through both experimentation and theory. A system model was constructed, accounting for two of the largest uncertainty sources: motion-induced positioning errors and errors due to non-orthogonality of the interferometer axes. The model was evaluated using a simple Monte Carlo method, with qualitatively satisfying results. Standard uncertainty components for XYZ-position were computed for a generated data-set representing a 2D lattice. Uncertainty components lie in the nm range, which is indicative of applicability to nanoscale measurements. The model should next be extended to also compute a measurand - a quantity of interest - related to transfer standards. With this extension, the model should provide an efficient way to obtain a MAFM measurement's uncertainty.

References

- [1] J. C. for Guides in Metrology. *JCGM 100:2008 : Evaluation of measurement data — Guide to the expression of uncertainty in measurement*. Tech. rep. JCGM, 2008.
- [2] P. Ceria et al. “Modelling of the X,Y,Z positioning errors and uncertainty evaluation for the LNE’s mAFM using the Monte Carlo method”. In: *Measurement Science and Technology* 28.3 (Jan. 2017), p.034007. DOI: 10.1088/1361-6501/28/3/034007.
- [3] J. C. for Guides in Metrology. *JCGM 101:2008 : Evaluation of measurement data — Supplement 1 to the “Guide to the expression of uncertainty in measurement” — Propagation of distributions using a Monte Carlo method*. Tech. rep. JCGM, 2008.
- [4] EMPiR. *Traceable three-dimensional nanometrology - 3DNano*. Website accessed 21.12.2018. 2016-2019. URL: <https://www.ptb.de/emrp/15sib09-project.html>.
- [5] J. C. for Guides in Metrology. *International vocabulary of metrology — Basic and general concepts and associated terms (VIM)*. Tech. rep. JCGM, 2008.
- [6] T. J. Quinn. “Practical realization of the definition of the metre, including recommended radiations of other optical frequency standards (2001)”. In: *Metrologia* 40.2 (Apr. 2003), pp. 103–133. DOI: 10.1088/0026-1394/40/2/316.
- [7] A. C. L. M. P. D. A.A. Madej J.E Bernard and K. J. Siemsen. “From Chains to Short Pulses: Absolute Frequency Measurements Across the Optical Spectrum”. In: *n/a*. 2003.
- [8] V. Korpelainen. “Traceability for nanometre scale measurements : Atomic force microscopes in dimensional nanometrology”. PhD thesis. Department of Physics, University of Helsinki, 2014.

- [9] K. Harding. *Handbook of Optical Dimensional Metrology*. CRC Press, Apr. 19, 2016. 506 pp. URL: https://www.ebook.de/de/product/21178054/handbook_of_optical_dimensional_metrology.html.
- [10] J. Seppä et al. “A method for linearization of a laser interferometer down to the picometre level with a capacitive sensor”. In: *Measurement Science and Technology* 22.9 (Aug. 2011), p. 094027. DOI: 10.1088/0957-0233/22/9/094027.
- [11] V. Korpelainen. “Acoustic method for determination of the effective temperature and refractive index of air in accurate length interferometry”. In: *Optical Engineering* 43.10 (Oct. 2004), p. 2400. DOI: 10.1117/1.1787834.
- [12] G. Binnig, C. F. Quate, and C. Gerber. “Atomic Force Microscope”. In: *Physical Review Letters* 56.9 (Mar. 1986), pp. 930–933. DOI: 10.1103/physrevlett.56.930.
- [13] T. Akiyama et al. “Symmetrically arranged quartz tuning fork with soft cantilever for intermittent contact mode atomic force microscopy”. In: *Review of Scientific Instruments* 74.1 (Jan. 2003), pp. 112–117. DOI: 10.1063/1.1523631.
- [14] A. Yacoot and L. Koenders. “Aspects of scanning force microscope probes and their effects on dimensional measurement”. In: *Journal of Physics D: Applied Physics* 41.10 (Apr. 2008), p. 103001. DOI: 10.1088/0022-3727/41/10/103001.
- [15] D. Ziegler et al. “Ideal Scan Path for High-Speed Atomic Force Microscopy”. In: *IEEE/ASME Transactions on Mechatronics* 22.1 (Feb. 2017), pp. 381–391. DOI: 10.1109/tmech.2016.2615327.
- [16] D. J. Whitehouse. *Handbook of Surface and Nanometrology*. CRC Press, Dec. 23, 2010. 999 pp. ISBN: 1420082019. URL: https://www.ebook.de/de/product/7186565/david_j_whitehouse_handbook_of_surface_and_nanometrology.html.
- [17] V. Korpelainen, J. Seppä, and A. Lassila. “Design and characterization of MIKES metrological atomic force microscope”. In: *Precision Engineering* 34.4 (Oct. 2010), pp. 735–744. DOI: 10.1016/j.precisioneng.2010.04.002.

- [18] V. Korpelainen. “Measurement strategies and uncertainty estimations for pitch and step height calibrations by metrological atomic force microscope”. In: *Journal of Micro/Nanolithography, MEMS, and MOEMS* 11.1 (Feb. 2012), p. 011002. DOI: 10.1117/1.jmm.11.1.011002.
- [19] I. Misumi et al. “Uncertainty in pitch measurements of one-dimensional grating standards using a nanometrological atomic force microscope”. In: *Measurement Science and Technology* 14.4 (Mar. 2003), pp. 463–471. DOI: 10.1088/0957-0233/14/4/309.
- [20] R. Dixson et al. “Spatial dimensions in atomic force microscopy: Instruments, effects, and measurements”. In: *Ultramicroscopy* 194 (Nov. 2018), pp. 199–214. DOI: 10.1016/j.ultramic.2018.08.011.
- [21] M. Fouchier, E. Pargon, and B. Bardet. “An atomic force microscopy-based method for line edge roughness measurement”. In: *Journal of Applied Physics* 113.10 (Mar. 2013), p. 104903. DOI: 10.1063/1.4794368.
- [22] R. Kizu et al. “Development of a metrological atomic force microscope with a tip-tilting mechanism for 3D nanometrology”. In: *Measurement Science and Technology* 29.7 (May 2018), p. 075005. DOI: 10.1088/1361-6501/aabe1a.
- [23] A. B. Owen. *Monte Carlo theory, methods and examples*. n/a, 2013.
- [24] E. Abbe. “Beiträge zur Theorie des Mikroskops und der mikroskopischen Wahrnehmung”. In: *Archiv für Mikroskopische Anatomie* 9.1 (Dec. 1873), pp. 413–418. DOI: 10.1007/bf02956173.
- [25] R. P. Paul. *Robot Manipulators: Mathematics, Programming, and Control (Artificial Intelligence)*. The MIT Press, 1981. ISBN: 9780262160827. URL: <https://www.amazon.com/Robot-Manipulators-Mathematics-Programming-Intelligence/dp/026216082X?SubscriptionId=AKIAIOBINVZYXZQZ2U3A&tag=chimbiori05-20&linkCode=xm2&camp=2025&creative=165953&creativeASIN=026216082X>.
- [26] G. Zhang. “A Study on the Abbe Principle and Abbe Error”. In: *CIRP Annals* 38.1 (1989), pp. 525–528. DOI: 10.1016/s0007-8506(07)62760-7.
- [27] R. Köning, J. Flügge, and H. Bosse. “A method for the in situ determination of Abbe errors and their correction”. In: *Measurement Science and Technology* 18.2 (Jan. 2007), pp. 476–481. DOI: 10.1088/0957-0233/18/2/s21.

- [28] K. Dirscherl. “Online correction of scanning probe microscopes with pixel accuracy”. English. PhD thesis. Technical University of Denmark, 2000.
- [29] D. Jurman et al. “Calibration and data fusion solution for the miniature attitude and heading reference system”. In: *Sensors and Actuators A: Physical* 138.2 (Aug. 2007), pp. 411–420. DOI: 10.1016/j.sna.2007.05.008.
- [30] M. Sonka, V. Hlavac, and R. Boyle. *Image Processing, Analysis, and Machine Vision*. CENGAGE LEARNING, Jan. 1, 2014. 869 pp. ISBN: 1133593607. URL: https://www.ebook.de/de/product/21323846/milan_sonka_vaclav_hlavac_roger_boyle_image_processing_analysis_and_machine_vision.html.
- [31] H. Freeman and R. Shapira. “Determining the minimum-area encasing rectangle for an arbitrary closed curve”. In: *Communications of the ACM* 18.7 (July 1975), pp. 409–413. DOI: 10.1145/360881.360919.
- [32] J. Bennett et al. “Numerically stable, single-pass, parallel statistics algorithms”. In: *2009 IEEE International Conference on Cluster Computing and Workshops*. IEEE, 2009. DOI: 10.1109/clustr.2009.5289161.
- [33] C. M. Mate, M. R. Lorenz, and V. J. Novotny. “Atomic force microscopy of polymeric liquid films”. In: *The Journal of Chemical Physics* 90.12 (June 1989), pp. 7550–7555. DOI: 10.1063/1.456188.